

February 25<sup>th</sup>, 2020

Dear Dr. Maycock:

We would like to resubmit our paper, “Atmospheric Teleconnection Processes Linking Winter Air Stagnation and Haze Extremes in China with Regional Arctic Sea Ice Decline” (manuscript#: acp-2019-1023), for publication in the *Atmospheric Chemistry and Physics*. In the revised version of the manuscript, we have addressed all the concerns posed by the two referees and improved the presentation quality by adding new figures and rewriting several parts in the manuscript.

The major changes in the revised manuscript include:


- (1) Replotted Fig.3/5/6 in the main text and new Fig. S7/S8 in the Supplement. These figures are improved/added according to the referee#1’s suggestions.
- (2) More discussion about the interpretation of our modeling results and its implications. These changes are made to address the referee#2’s major concern.

Please see the responses to the referees and the revised manuscript with tracked changes in this file for details. A clean version of the revised manuscript without tracked changes and a new supplement file are also uploaded to the online submission system.

We believe the revised manuscript represents better presentation and justification of our work and would like to resubmit it for your consideration. We appreciate the time and efforts you and the referees put into reviewing this paper.

I look forward to hearing from you again.

Sincerely,



Yufei Zou

Postdoctoral Research Associate  
Atmospheric Sciences and Global Change Division  
Pacific Northwest National Laboratory  
902 Battelle Blvd  
Richland, WA 99354  
Email: [yufei.zou@pnnl.gov](mailto:yufei.zou@pnnl.gov)

Response to Referee #1:

#### GENERAL COMMENTS

This paper uses climate model experiments in which regional Arctic sea-ice decline is imposed, combined with analysis of new CMIP6 data, to better understand the dynamical mechanisms by which Arctic sea-ice decline may influence winter haze pollution extremes in China. The main new result reported is that Pacific sector sea-ice loss increases the likelihood and intensity of haze pollution extremes, due to anomalous transient eddy vorticity fluxes amplifying the negative phase of the EU pattern.

Given the substantial impact of haze pollution extremes on public health, this study represents an important contribution to this research area. The variety of methods used – including targeted single model experiments, new CMIP6 multi-model data, and a variety of interesting diagnostics – is also good. The paper is generally well presented with a good quality and number of figures, and only minor alterations are required to the wording and structure.

However, while this study reports potentially very interesting and impactful results, I am concerned about the statistical robustness of some of the conclusions and, therefore, that the length of the simulations (30 years) may be too short. My specific comments below explain these concerns in detail, which I would like to see addressed.

Response: Thank you very much for the constructive comments and suggestions. We understand your concerns about the robustness of the modeling results in the manuscript. Therefore, we have conducted additional statistical significance tests to demonstrate that these results are robust. We also revised the manuscript to address your other concerns. Please see below our responses (in blue) to your specific comments.

#### SPECIFIC COMMENTS

Page 1, line 19: I found the use of the word ‘event’ a bit confusing in this study, as the extremes analysed are monthly extremes and ‘event’ – to me anyway – implies a shorter timescale (daily or weekly). It would be helpful to clarify somewhere what is meant by the term ‘event’ here, or to avoid using the term.

Response: Thank you for the suggestion. Since there are many different types of climate extreme events such as cold extremes, heatwaves, droughts, and extreme precipitation, etc., we want to emphasize here that pollution-related air stagnation extremes are the major focus of this study. To avoid possible confusion with time scale-related interpretation, we rephrased the expression here to “monthly air stagnation extremes” and revised all similar expressions throughout the manuscript.

Introduction: This paragraph is far too long, which made the structure of the introduction – which while good – a bit hard to follow. Breaking this up into a few paragraphs would help. The same goes for similarly long paragraphs in other parts of the paper (e.g. page 4 lines 9-40; page 9).

Response: We have followed the suggestion to break those long paragraphs into shorter ones on page 2, page 4, and page 9. Please see the revised manuscript for details.

Page 2, lines 32-35: This sentence is a bit misleading, as it implies that there is a scientific consensus that high-latitude climate change influences mid-latitude circulation and weather, when there is not (e.g. <https://www.nature.com/articles/s41558-019-0662-y>). There is lots of evidence suggesting that Arctic sea-ice loss can have an influence on mid-latitudes, but whether it has in the past or will in the future is more unclear (<https://onlinelibrary.wiley.com/doi/full/10.1002/wcc.337>). Would be good to rephrase the sentence to reflect this (e.g. ‘Given the increasing evidence that climate change – especially that occurring in high-latitude regions – may have an influence on middlelatitude circulation’).

Response: We agree that there are lots of discussion and ongoing debates on this topic. Knowledge gaps regarding complex interactions between high-latitude and mid-latitudes and physical pathways behind these phenomena still exist. A few climate modeling studies have been conducted to narrow down the uncertainty associated with the influence of high-latitude climate change on mid-latitude weather extremes. Our study was motivated and inspired by these discussions and modeling efforts. To clarify on the current research status, we have rephrased the text as suggested and added more specific discussion and references in lines 2-5 of page 3:

“Several possible dynamic pathways linking Arctic warming to midlatitude weather extremes have been proposed and investigated in the past few years (Barnes and Screen, 2015; Overland et al., 2016). However, the observational data and modeling results are sometimes contradictory and are open to different interpretations (Cohen et al., 2020)”.

Section 2.1: I found this section jumped around a bit in terms of the definitions of the EU pattern and index, the MCA\_Z500 pattern, and the PPI. If possible, could this be restructured so that the definition of each is closer to where it is originally introduced?

Response: Thank you for the suggestion. We revised this section to more clearly describe all the indices used in the manuscript. Please see Section 2.1 in the revised manuscript for details.

Page 3, lines 29-30: It would be helpful to properly explain and define the WSI and ATGI.

Response: The two indices are defined and explained in lines 34-37 of page 3:

“WSI was standardized by subtracting time-averaged climatological mean of near-surface wind speed over the 1981-2010 period from the monthly values at each grid cell and then dividing by its standard deviations in the same period. ATGI was the standardized potential temperature gradient field between 925 and 1000 hPa using the same method. These two indices are used to reflect horizontal and vertical dispersions of near-surface air pollutants, respectively.”

Page 4, lines 3-5: Do you have a citation for this?

Response: This statement is based on the similarity between MCA\_Z500 and EU as well as other teleconnection patterns such as the East Atlantic (EA) pattern ([https://www.cpc.ncep.noaa.gov/data/teledoc/ea\\_map.shtml](https://www.cpc.ncep.noaa.gov/data/teledoc/ea_map.shtml)) and the East Atlantic/Western Russia (EA/WR) pattern (<https://www.cpc.ncep.noaa.gov/data/teledoc/eawruss.shtml>) over East Asia in winter (e.g., January patterns), as shown in Fig. R1.

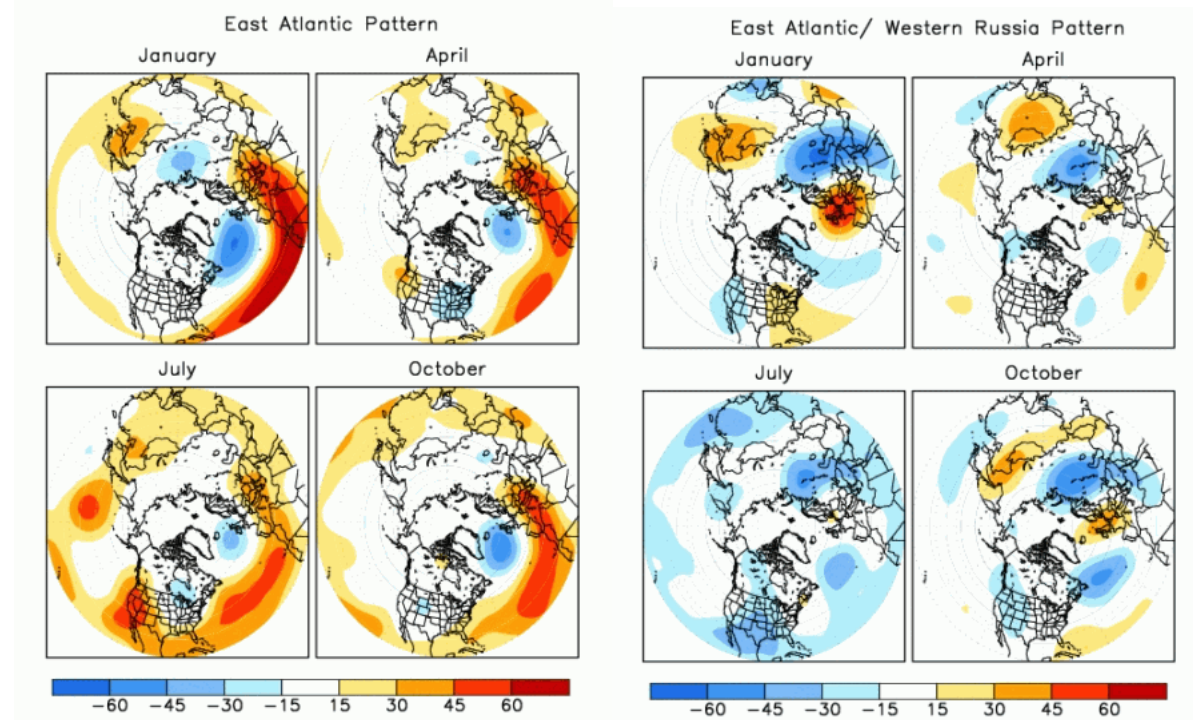


Figure R1: 500 hPa geopotential height anomalies (unit: m) of the East Atlantic pattern (left) and the East Atlantic/Western Russia pattern (right) in different months. These plots are adapted from the NOAA Climate Prediction Center (CPC) website (<https://www.cpc.ncep.noaa.gov/data/teledoc/telecontents.shtml>; last access: 14 February 2020).

The major difference between EU and other planetary-scale teleconnection patterns is in the wave propagation pathways in the upstream regions such as the Atlantic and Europe, while they share similar configurations in the downstream regions over East Asia. All these teleconnection patterns can be excited by either internal variability or localized forcings (Simmons et al., 1983; Sardeshmukh et al., 1988; Liu et al., 2014; Lim, 2015). To clarify this, we added examples and references in lines 15-18 of page 4 in the revised manuscript as:

“However, it’s worth noting that this regional MCA\_Z500 pattern can also be excited by other large-scale teleconnection processes such as the East Atlantic pattern or the East Atlantic/Western Russia pattern associated with both natural variability and perturbed Rossby wave activity (Lim, 2015; Simmons et al., 1983).”

Section 2.2: Are you able to justify using simulations of only 30 years in length? To me this seems rather short, especially considering my comments regarding statistical robustness below. Indeed, Screen et al. 2014 show that the simulated circulation response to sea-ice loss is small compared to internal variability (i.e. there is a low signal-to-noise ratio), and specifically that at least 70 year-long experiments are required to simulate a robust mid-tropospheric response

to sea-ice loss (<https://link.springer.com/article/10.1007/s00382-013-1830-9>). Similarly, simulations submitted to PAMIP (the Polar Amplification Model Intercomparison Project) are required to be at least 100 years long due to this low signal-to-noise ratio (<https://www.geosci-model-dev.net/12/1139/2019/>). Also, many studies using WACCM to investigate the response to sea-ice loss use longer simulations (e.g. England et al. 2019 use 151 years, <https://journals.ametsoc.org/doi/full/10.1175/JCLI-D-17-0666.1>; Sun et al. 2015 use 161 years, <https://journals.ametsoc.org/doi/full/10.1175/JCLI-D-15-0169.1>; Zhang et al. 2018 use 60 years, <https://advances.sciencemag.org/content/4/7/eaat6025>).

Response: Thank you for the comment and references. Several studies, including those in your comment, have indicated that the signal-to-noise ratio associated with the Arctic influence on midlatitude weather is lower than internal variability, which motivated the long-term simulations in those studies to try to isolate a robust atmospheric response in the middle latitudes to Arctic sea ice loss and Arctic amplification. However, most, if not all, Arctic-midlatitude impact studies focused on the response in ensemble seasonal mean state rather than monthly extreme values in our case. We want to emphasize that the modeling responses could be very different in terms of these two metrics. This is evident by comparing the changes in ensemble mean values (Table S2 in the Supplement) with those in extreme values (Table S3/S4 in the Supplement) of each sensitivity experiment. It can also be clearly demonstrated by the following conceptual changes in temperature distribution and their effects on extreme values (Fig. R2). In this IPCC report (2012), three distinct distribution changes in response to climate change have been proposed: shifted mean, increased variability, and changed symmetry, which suggest complex relationship between changes in ensemble mean and extreme values. We followed this analysis framework to characterize modeling responses in our climate sensitivity experiments and found the SENSr2 results of interest fall into the “Changed Symmetry” category (as shown in Fig. S2/S3 in the Supplement).



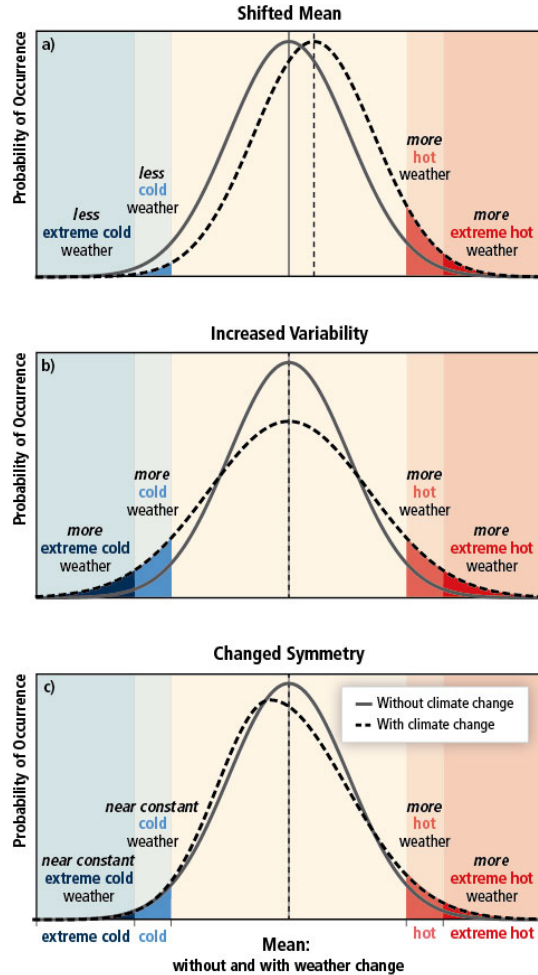


Figure R2: The effect of distribution changes on temperature extremes. Different changes in temperature distributions between present and future climate and their effects on extreme values of the distributions: (a) effects of a simple shift of the entire distribution toward a warmer climate; (b) effects of an increase in temperature variability with no shift in the mean; (c) effects of an altered shape of the distribution, in this example a change in asymmetry toward the hotter part of the distribution. This plot is adopted from Figure SPM. 3 in IPCC (2012).

To evaluate statistical significance of the changes in positive extreme probability, we repeatedly resample a subset of modeling years in SENSr2 for 10,000 times and then use a non-parametric kernel density estimation (KDE) function to re-estimate the probability of ECP\_PPI (Fig. R3) positive extremes in each subset comparing with their CTRL counterpart. We try two different methods of resampling: without replacement and with replacement for multiple subset sizes (10, 15, 20, 25, 30). Sampling without replacement does not allow duplicated modeling years while sampling with replacement generates much more combinations and larger variances of subsets. Since there are numerous combinations of resampled subsets (except the subset size of 30 years without replacement, which has only one unique combination of all data), we plot the empirical probability density distributions of positive extreme probabilities using kernel density estimation for each subset size (similar to Fig. 8 in Screen et al., 2014). Please note that the actual sample size in each subset should be multiplied by 3 because we use monthly data in winter (Dec-Jan-Feb) rather than seasonal average to detect climate extremes. For example, the total sampling size for the subset of 10 years is 3 months  $\times$  10 years = 30 months. The autocorrelation among these winter months is low and insignificant (please see the response to the next question for details).

After obtaining these empirical PDFs, we estimate the corresponding value of the CTRL positive extreme probability in these PDFs to test the hypothesis that the SENSr2 positive extreme probability is significantly larger than the CTRL run (the CTRL positive extreme probability is always 0.05 since the 95<sup>th</sup> percentile of CTRL data is

chosen as the positive extreme threshold). As shown in Fig. R3 below, the chance of SENSr2 ECP\_PPI positive extreme probability  $\leq$  CTRL ECP\_PPI positive extreme probability (0.05) is about 3% when the subset size exceeds 15 years (45 months) without replacement (Fig. R3a), or when the subset size exceeds 25 years (75 months) with replacement (Fig. R3b). Another way to demonstrate this is to plot the positive extreme probability estimates and their 95% percentile ranges against different ensemble sizes (Fig. R4; we updated Fig. S3/S4 in the supplement using the same method here), which suggest the same conclusion. The ensemble averaged estimates of the SENSr2 ECP\_PPI positive extreme probability are also quite similar among different ensemble sizes ( $\sim 0.11$ ) and more than double of the CTRL positive extreme probability (0.05). Therefore, we are confident that the current modeling simulation length of 30 years is long enough to detect significant extreme probability changes, which is the primary research objective of this study.

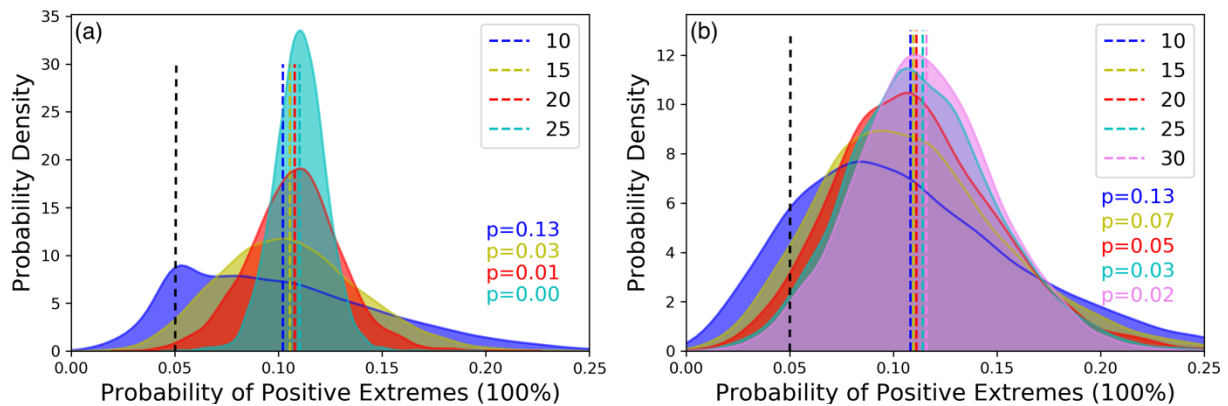


Figure R3: KDE-based probability estimates of ECP\_PPI positive extremes in SENSr2 based on different ensemble sizes of subsets (a) without and (b) with replacement in bootstrap resampling ( $n=10,000$ ). The p values on bottom-right corners are the probabilities of 0.05 (the CTRL positive extreme probability shown as the black dash line) in each PDF curve. The colored dash lines are ensemble averaged probabilities of SENSr2 positive extremes for each subset size. Note that no PDF curve is available for  $nsize=30$  without replacement in (a) because of the uniqueness of the sampling combination.

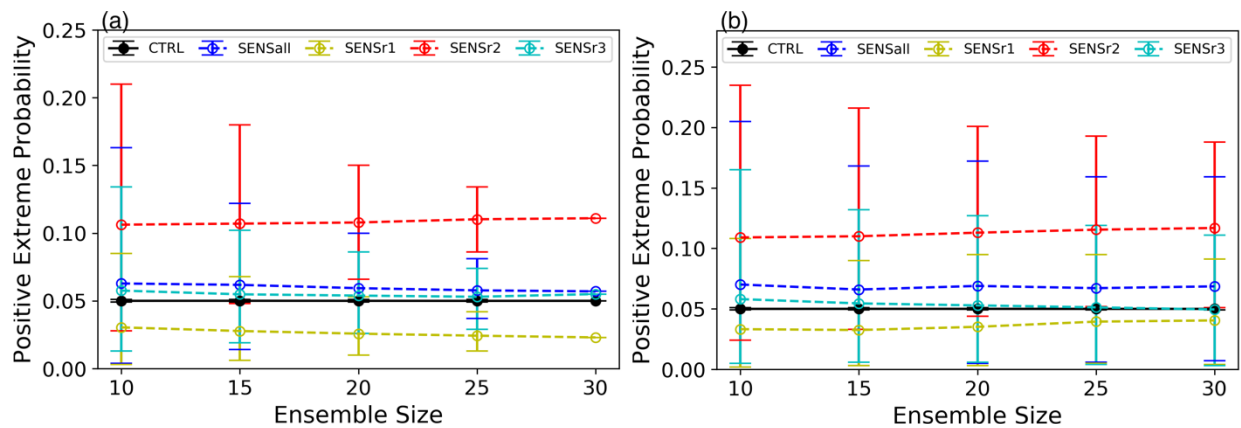


Figure R4: Comparison of KDE-based probability estimates of ECP\_PPI positive extremes based on different ensemble sizes of subsets (a) without and (b) with replacement in bootstrap resampling ( $n=10,000$ ). The error bars denote the 95% percentile range (2.5% to 97.5%) for positive extreme probability values at each ensemble size.

Page 6, lines 4-6: You say that you have 90 samples when conducting this statistical test, and so I presume you are assuming 90 degrees of freedom. However, have you checked whether the MCA\_Z500 and/or ECP\_PPI indices are autocorrelated (e.g. between consecutive months or lag-1), and therefore whether 90 degrees of freedom is an overestimate?

Response: Thank you for the suggestion. We can treat each sequence of monthly data in Dec, Jan, and Feb as three sampling groups. The essence of this question is whether two consecutive groups of monthly data are independent or not. We test the lag-1 relationship in both MCA\_Z500 and ECP\_PPI indices by checking the Pearson correlation coefficients between two consecutive monthly groups. If they are not independent from each other, then we would expect statistically significant correlations between these paired groups. Table R1 and Table R2 show the correlation coefficients for both indices and their corresponding two-tailed p-values, respectively, suggesting insignificant correlations in most MCA\_Z500 pairs and all ECP\_PPI pairs.

Table R1: Correlation coefficients of the MCA\_Z500 and ECP\_PPI indices between two consecutive months in each modeling experiment

r	MCA_Z500		ECP_PPI	
	Dec-Jan	Jan-Feb	Dec-Jan	Jan-Feb
CTRL	0.27	0.01	-0.02	-0.28
SENSall	0.43	0.05	0.24	0.19
SENSr1	0.003	0.28	-0.04	-0.03
SENSr2	0.17	0.53	0.07	-0.17
SENSr3	0.25	0.03	0.14	-0.23

Table R2: Two-tailed p-value of the MCA\_Z500 and ECP\_PPI correlation coefficients between two consecutive months in each modeling experiment

p-value	MCA_Z500		ECP_PPI	
	Dec-Jan	Jan-Feb	Dec-Jan	Jan-Feb
CTRL	0.15	0.95	0.90	0.14
SENSall	0.02	0.81	0.20	0.31
SENSr1	0.99	0.14	0.84	0.87
SENSr2	0.37	0.003	0.72	0.37
SENSr3	0.18	0.86	0.47	0.22

Since the Pearson correlation coefficient is highly sensitive to outliers, we also plot the scatter plots based on the winter consecutive monthly MCA\_Z500 data in SENSall and SENSr2 that show possible correlations. As shown in the plots, the Pearson correlations are mainly contributed by two MCA\_Z500 outliers (in the red circle) on bottom-left corners between December and January in SENSall (Fig. R5a), and one MCA\_Z500 outlier (in the red circle) on top-right corner between January and February in SENSr2 (Fig. R6b). After removing these outliers, the correlations would largely decrease to insignificant levels (SENSall:  $r=0.13$ ,  $p=0.52$ ); SENSr2:  $r=0.36$ ,  $p=0.06$ ) after removing the outliers in red circles). Another way to show the large impact of outliers on the Pearson correlation coefficients is to use the non-parametric Kendall rank correlation as an alternative, which is more suitable for small sample sizes without the Gaussian distribution assumption. The Kendall rank correlation coefficients for these MCA\_Z500 data in Dec-Jan of SENSall and Jan-Feb of SENSr2 are  $(r=0.16, p=0.23)$  and  $(r=0.26, p=0.04)$ , respectively. Both are much smaller than the Pearson ones listed in the above tables. Actually, the lifetime of most severe pollution events is shorter than one month, and the memory effect of the atmosphere is also short. Therefore, we feel it's acceptable to treat these monthly data as independent samples and the degree of freedom of 90 is considered a roughly accurate estimate for the statistical tests in the manuscript.

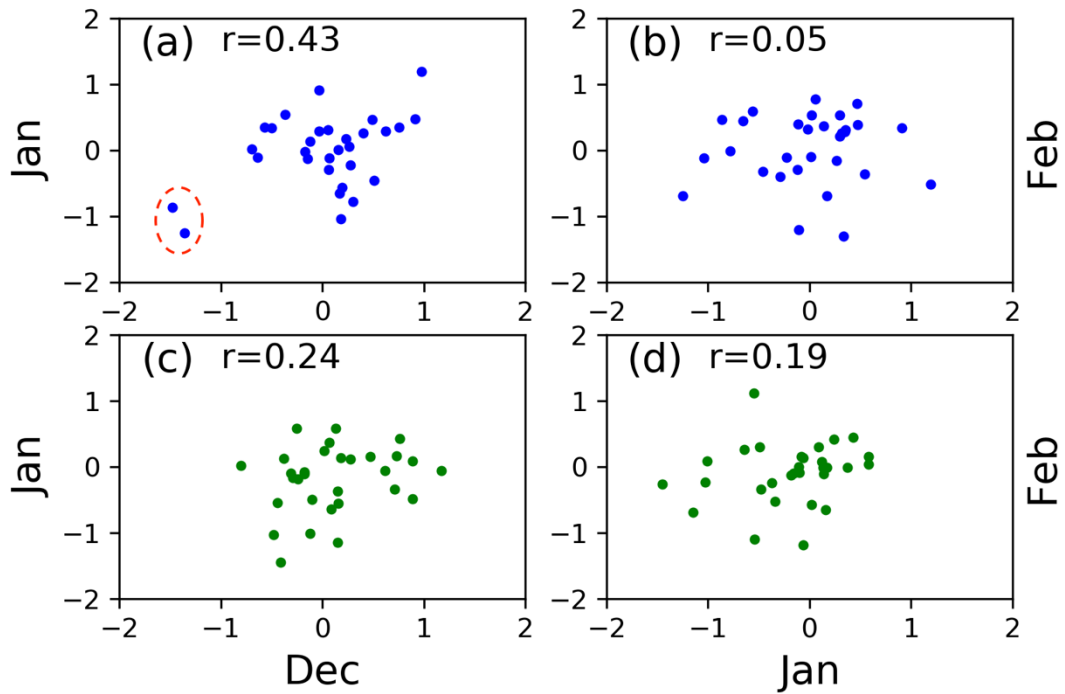


Figure R5: Scatter plots for the MCA\_Z500 and ECP\_PPI indices in consecutive months of the SENSall experiment. (a) the paired MCA\_Z500 indices in December and January; (b) the paired MCA\_Z500 indices in January and February; (c) the paired ECP\_PPI indices in December and January; (d) the paired ECP\_PPI indices in January and February. The red circle in (a) shows the outliers contribute largely to the Pearson correlation coefficient.

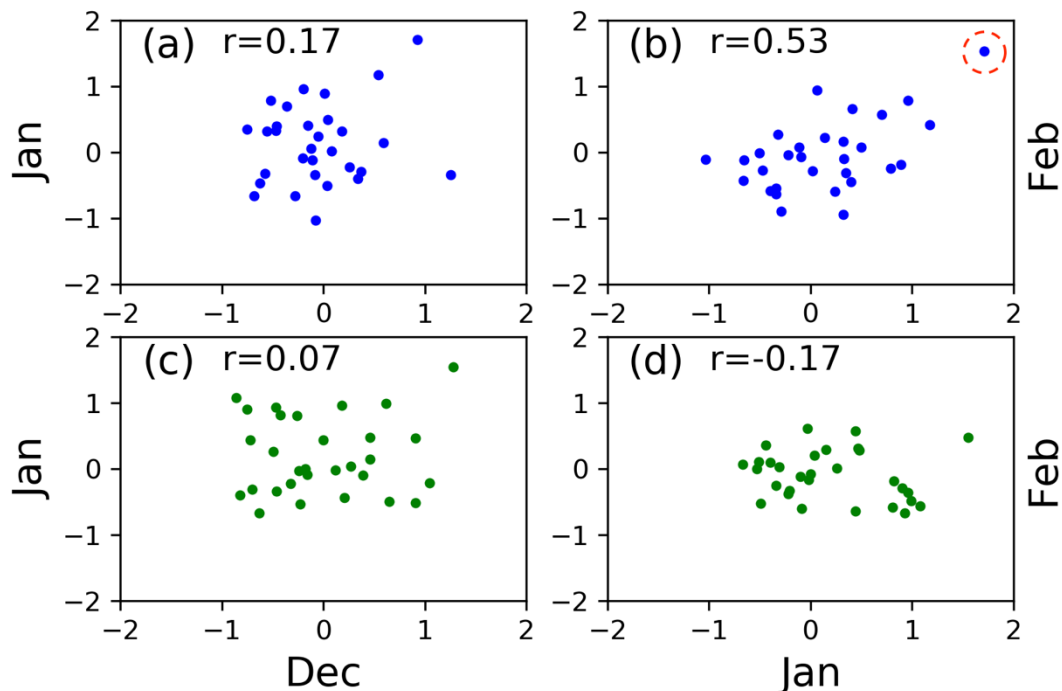


Figure R6: Scatter plots for the MCA\_Z500 and ECP\_PPI indices in consecutive months of the SENSr2 experiment. (a) the paired MCA\_Z500 indices in December and January; (b) the paired MCA\_Z500 indices in January and February; (c) the paired ECP\_PPI indices in December and January; (d) the paired ECP\_PPI indices in January and February. The red circle in (b) shows the outlier contributes largely to the Pearson correlation coefficient.

Page 6, lines 36-39: Relating to the above comment, did you account for autocorrelation when conducting this bootstrapping method (e.g. as done in your previous paper using the moving blocks method <https://advances.sciencemag.org/content/3/3/e1602751>)? If there is autocorrelation it may be that the uncertainties given by the bootstrap method (Tables S3 and S4) may be underestimated, and therefore the statistical robustness of the differences between the perturbation and CTRL experiments overestimated.

Response: As shown in our response to the previous comment, the autocorrelation in monthly data is negligible in most cases. Therefore, we used the standard bootstrapping method in this manuscript. The reason we used the moving block bootstrap method in our previous study (Zou et al., 2017) is that we used daily data in that study. The autocorrelation problem in these daily time series is much more severe than the monthly data used in this study, so the moving block bootstrap method was applied there. For the monthly data with less concern about autocorrelation, the standard bootstrap method was applied in the previous study (Zou et al., 2017) that is the same with the practice here.

Page 8, lines 21-23: It should be noted that these correlations are not statistically significant at most grid points (but perhaps the correlation would be significant if you used an area average?).

Response: This figure helps to identify the Arctic sub-regions with potential influence on the atmospheric teleconnection as well as regional ventilation in China. If averaging SIC over those R2 areas with positive correlations with the EU index, the regional averaged SIC-EU correlation coefficient is  $r=0.38$  ( $p=0.02$ ), which is statistically significant at the 0.05 significance level. We added this regional averaged correlation to lines 3-4 of page 9 in the revised manuscript.



Page 9, lines 20-23; Tables S3 and S4: Can you justify why you use the standard deviation here? The numbers in these tables for the SENSr2 experiment contain one of key results of this paper, suggesting that there is an increase in the likelihood and intensity of MCA\_Z500 and ECP\_PPI positive extremes in response to sea-ice loss in the R2 region. However, by using just the standard deviation it maybe cannot be said that the extremes in SENSr2 are significantly different statistically from those in CTRL.

I may be wrong, but a 95% confidence interval seems more appropriate to test whether the difference is statistically robust? Since a 95% confidence interval will be larger, the 9% 3% figure in Table S3 for SENSr2 MCA\_Z500 may not actually be significantly different from CTRL (5% 0%).

Response: Thank you for the suggestion. We redid the bootstrap analysis with replacement for 10,000 times to estimate the 95% percentile range for all the indices listed in Table S3 and Table S4. Please see below the updated tables (we included here for your convenience):

Table S3. The bootstrap (nboot=10000) estimates (ensemble mean and 95% percentile range) of positive extreme probabilities of the MCA\_Z500 and ECP\_PPI indices in the WACCM experiments

	CTRL	SENSall	SENSr1	SENSr2	SENSr3
MCA_Z500	5.0%	3.7% (0-13.5%)	3.3% (0-9.2%)	7.5% (0.8-16.4%)	4.1% (0-12.8%)
ECP_PPI	5.0%	7.0% (0.7-16.1%)	4.1% (0.4-9.2%)	11.6% (5.2-18.4%)	5.0% (0.2-11.0%)

Table S4. The bootstrap (nboot=10000) estimates (ensemble mean and 95% percentile range) of positive extreme intensities of the MCA\_Z500 and ECP\_PPI indices in the WACCM experiments

	CTRL	SENSall	SENSr1	SENSr2	SENSr3
MCA_Z500	1.14 (0.75-1.72)	1.00 (0.77-1.35)	1.07 (0.81-1.44)	1.27 (0.90-1.68)	1.03 (0.77-1.41)
ECP_PPI	0.86 (0.63-1.40)	0.91 (0.70-1.25)	0.94 (0.72-1.31)	1.12 (0.90-1.42)	0.84 (0.66-1.13)

The new estimates don't change our conclusion in the manuscript, suggesting significantly increased probability and intensity of ECP\_PPI in SENSr2. This is also evident in Fig. R3b of the previous response. The increase in MCA\_Z500 is less significant than that in ECP\_PPI, which might be attributed to the smaller signal-to-noise ratio in large-scale dynamic processes. Extended climate sensitivity experiments could be conducted in the future to evaluate the robustness of these large-scale dynamic responses.

Page 9, line 23 to page 10, line 28: Results relating to changes in the ensemble mean of the MCA\_Z500 and ECP\_PPI indices are presented and discussed as if they are statistically robust (e.g. 'The differences in the MCA\_Z500 and ECP\_PPI responses among the four sensitivity experiments in extreme members and ensemble means also suggest complex relationships between Arctic sea ice loss and mid-latitude weather changes'). However, they are only statistically significant for SENSr1 ECP\_PPI ( $p=0.04$ ) – see Table S2. These paragraphs should be edited so that is clear whether the results being presented and discussed are robust or not.

Response: We rewrote the paragraphs to clearly indicate the robustness of changes in both ensemble mean and extreme values of both indices. Please see below the updated paragraphs in Section 3.2 of the revised manuscript.

"To examine the regional circulation and ventilation responses to these changes in the high latitudes, we fit the CDF and PDF curves of MCA\_Z500 and ECP\_PPI based on CTRL and SENS monthly results in winter. Figure 3 shows the CDF changes of simulated MCA\_Z500 (Fig. 3a) and ECP\_PPI indices (Fig. 3b) between sensitivity and CTRL experiments. It is clear that both indices show more significant changes in their extreme members than in medians or ensemble means, especially in SENSr2 driven by SIC and SST changes in the Pacific sector of the Arctic (R2 in Fig. 1b). In SENSr2, the occurrence probability of MCA\_Z500 positive extremes increases by 50% from 5.0 to 7.5% (95<sup>th</sup> percentile range: 0.8-16.4%) (Fig. 3a; Table S3 in the Supplement), while the ECP\_PPI positive extremes increases by 132% to 11.6% (95% percentile range: 5.2-18.4%) (Fig. 3b; Table S3 in the Supplement). Meanwhile, the intensity of positive extreme values of the two indices also increases by 11% and 30%, respectively

(Table S4 in the Supplement). The increase in the teleconnection pattern index MCA\_Z500 is less significant than that in the regional air stagnation index ECP\_PPI, suggesting a potential nonlinear relationship between large-scale circulation and regional stagnation. Only SENSr2 shows statistically significant increases of ECP\_PPI in terms of positive extreme probability and intensity, and the significance of such increases is independent from the fitting method being used (i.e., still valid with nonparametric curve fitting). The substantially increased positive extremes in SENSr2 contribute to the positive responses in its ensemble mean, making SENSr2 the only sensitivity experiment with positive ensemble mean ECP\_PPI (0.03, not statistically significant). In comparison, other SENS experiments generally show negative ensemble mean ECP\_PPI values due to left-shifted CDF curves at most percentiles. For instance, SENSr1 is the only experiment showing robustly decreased ECP\_PPI at all percentiles in its CDF curve (Fig. 3b), contributing to its negative ensemble mean of ECP\_PPI (-0.13) that is statistically significant at the 0.05 significance level (Table S2 in the supplement). This result implies an overall improvement of the ECP regional ventilation driven by the SIC and SST changes in the Barents-Kara Seas (R1 in Fig. 1b), while the ventilation responses are more random driven by sea ice loss in other Arctic regions.”

Section 3.4: Why has only the ECP\_PPI index been calculated for the CMIP6 results, and not the MCA\_Z500 index, when both were for the WACCM results? This seems quite key, since it is MCA\_Z500 that demonstrates a dynamical (and therefore more causal) connection between sea-ice loss and ECP\_PPI.

Response: Thank you for the suggestion. We have now added the time series and changes of MCA\_Z500, based on the reanalysis and CMIP6 results, in a new supplementary Figure S8 (shown as Fig. R7 here). The MCA\_Z500 projection results also show right-shifted positive extremes in future time periods, with the largest shift emerging during the P3 period in concurrence with the strongest decline of Arctic sea ice. Please see Section 3.4 in the revised manuscript for details.

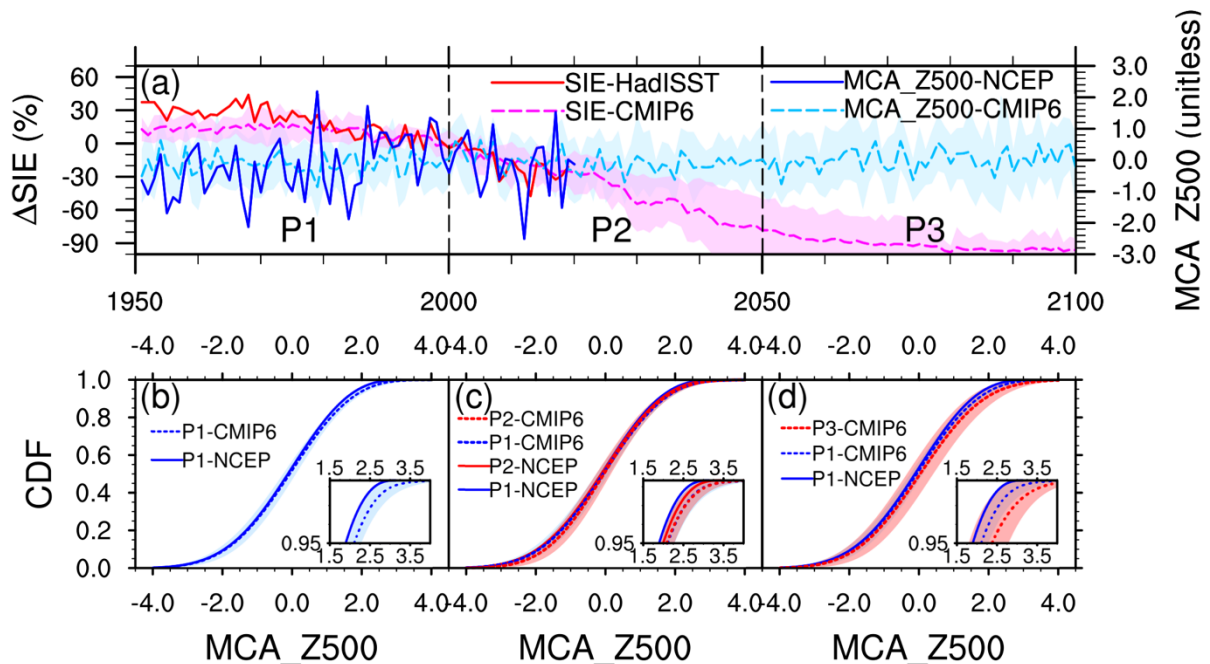


Figure R7. Historical simulations and future projections (under the SSP5-8.5 scenario) of Arctic sea ice and regional circulation in observational and reanalysis data and CMIP6 models. (a) time series of the Arctic SIE relative changes (unit: %; relative to 1981-2010) in preceding September and MCA\_Z500 (unitless) in DJF of the following winter (using years of January for X-axis labeling). The solid lines denote observation- and reanalysis-based Arctic SIE and MCA\_Z500 from 1950 to 2019. The dashed lines denote ensemble mean and the color shading denotes  $\pm 1$  standard deviation of the 8 CMIP6 models (see Table S1 for model details) from 1950 to 2100. Note that the SIE time series were shifted forward by one year to align with the MCA\_Z500 data; (b) comparison of MCA\_Z500 CDF curves between the NCEP reanalysis data and the CMIP6 models in the P1 time period from 1951 to 2000. The inset

denotes the distributions of positive extremes ( $\geq MCA\_Z500_{P1}^{95th}$ ). The color shading denotes  $\pm 1$  standard deviations in the 8 CMIP6 models; (c) Same as (b) but for the comparison between P1 and P2 (2001-2050) time periods as well as between the NCEP reanalysis data and the CMIP6 models; (d) same as (b) but for the comparison between P1 and P3 (2051-2100) time periods as well as between the NCEP reanalysis data and the CMIP6 models.

Figure 1, Figure S1, Figure 5 (a) and (c): It would be useful to indicate in the captions that these plots are for observational/reanalysis data, rather than for the sensitivity experiments conducted. For Figure 5 (a) and (c) specifically this is mentioned initially, but it would be clearer to say this in the caption after (a) and (c) as well.

Response: We add the descriptions in the figure captions as suggested.

Figure 3: In the caption it says ‘Atmospheric circulation and regional air stagnation responses to the Arctic sea ice forcing in the WACCM experiments’. However, what is in the figure is the absolute CDFs for the CTRL and SENS experiments, rather than differences between the SENS experiments and CTRL (what is normally defined as the ‘response’). The use of ‘response’ in the caption is therefore confusing and should be changed.

Response: We change the description here to “Comparison of the statistical distributions of atmospheric circulation and regional air stagnation indices in the WACCM climate sensitivity experiments” for clarification.

Figure 4: Since these plots show the difference between the SENSr2 extreme members and the CTRL ensemble mean, rather than the CTRL extreme members, these plots do not just show the effect of the sea-ice forcing imposed, but the combined effect of sea-ice loss and internal variability (which causes extreme events without the need for sea-ice loss). The start of the caption (‘Winter atmospheric response to the autumn and early winter sea ice change : :’) should therefore be re-phrased. Also - presumably ‘winter’ means the ‘winter mean’ here?

Response: Thank you for the suggestion. We rephrase the Fig.4 caption to “Atmospheric anomalies in WACCM SENSr2 extreme members with respect to the CTRL ensemble mean”. These extreme members spread in different winter months. Here the anomalies are based on the differences between the average of these extreme members and the CTRL average.

In the dynamic diagnosis part, we attempt to answer the following two questions:

- (1) How does severe air stagnation occur in these SENSr2 extreme members?
- (2) Why are there more and intensified air stagnation extremes in SENSr2?

As indicated by your comments, the extreme weather in these ensemble members could result from interactions between atmospheric internal variability and Arctic sea ice forcing. And we do find constructive interference between sea ice-related anomalous wave activity and the background flow (Fig. S7 in the supplement). Therefore, we use Fig. 4 in combination with the following figures (Fig. 5/6 in the revised manuscript) to answer the first question, and then use Fig. 5/6 and Fig. S7 in the supplement to answer the second question. Please see Section 3.3 of the revised manuscript for detailed analysis.

Figure 5: Why is there stippling to show statistical significance in all figures except this one?

Response: We didn’t add stippling to this figure in the previous version because it already has 3 layers (shading, contour, and vectors). Adding stipples would further increase its complexity. In the revised manuscript, we update Fig. 5 in the manuscript by separating the SENSr2 extreme members from their CTRL counterparts and adding stipples for significance tests in each subplot as suggested (shown as Fig. R8 here). A new figure is also added in the supplement (Fig. S7) to isolate the difference between the SENSr2 extreme members and their CTRL counterparts directly (SENSr2<sub>extreme</sub>-CTRL<sub>counterpart</sub>).

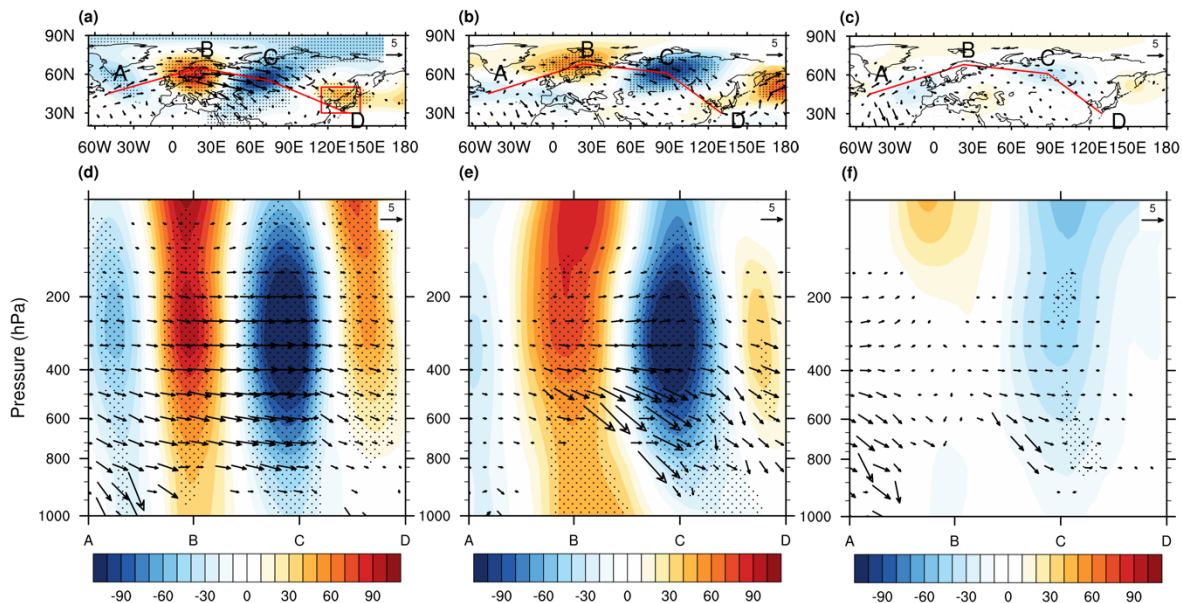


Figure R8: Comparison of atmospheric anomalies in the NCEP reanalysis data and WACCM experiments. (a) reanalysis-based ensemble mean geopotential heights at 500 hPa (color shading, m) and wave activity flux (WAF) at 250 hPa (vectors,  $\text{m}^2 \text{s}^{-2}$ ) of the 30 strongest negative EU months in winter (DJF) of 1951-2019 (relative to 1981-2010 climatology); (b) same as (a) but based on the SENSr2 extreme members (relative to CTRL ensemble mean); (c) same as (b) but based on the CTRL counterparts of the SENSr2 extreme members (relative to CTRL ensemble mean); (d) reanalysis-based vertical cross section of geopotential heights (color shading, m) and WAF (vectors,  $\text{m}^2 \text{s}^{-2}$ ) of the ensemble mean negative EU months along the wave propagation path shown in (a); (e) same as (d) but based on the SENSr2 extreme members (relative to CTRL ensemble mean); (f) same as (e) but based on the CTRL counterparts of the SENSr2 extreme members (relative to CTRL ensemble mean). Note that the vertical components of WAF in (c)-(d) were scaled up by 200 for clear illustration. The stipples denote the 0.05 significance level.

Figure S4: ‘Relative changes’ to what?

Response: Here the “relative changes” are changes in terms of percentages rather than absolute values. These percentages are calculated based on the relative concentration differences in SENS extreme members using the CTRL ensemble mean concentration as benchmark. For clarification, we rephrase the Fig. S4 caption to “Spatial distributions of surface  $\text{PM}_{2.5}$  concentration percentage changes (unit: 100%) in extreme members of each sensitivity experiment relative to the CTRL ensemble mean result”. Fig. S4c is used for direct comparison with Fig. S5 to demonstrate the effectiveness of PPI.

#### TECHNICAL CORRECTIONS

Page 3, line 23: Perhaps refer to ‘Fig 1 (c) and (d)’ instead of just ‘Fig 1’, since not referring to whole figure. If there are similar instances in other parts of the paper, could you perhaps change these too for clarity (e.g. page 4, line 1: ‘Fig S1 (b)’ rather than just ‘Fig S1’).

Response: Thank you for the suggestion. We change the references to specific subplots in the revised manuscript.

Page 3, line 33: I’m not sure the definition of  $\text{PM}_{10}$  would be immediately obvious to all readers, although I could be wrong. Perhaps consider including a very brief definition?

Response: The definitions of PM<sub>2.5</sub> “(particulate matter with aerodynamic diameters of 2.5 micrometers or less)” and PM<sub>10</sub> “(particulate matter with aerodynamic diameters of 10 micrometers or less)” have been added after its first appearance in line 7 and line 9 of page 2.

Page 6, line 11: ‘these’ should be ‘those’

Response: Thank you. It’s changed to “those”.

Page 9, line 24: ‘of two indices’ should be ‘of the two indices’

Response: Thank you. It’s changed as suggested.

Figures 3 and 7: ‘inlet’ should be ‘inset’

Response: Thank you. All typos have been changed to “inset” in the captions of Fig. 3 and Fig. 7.

Figure 6 (a) and (b): This rainbow colour scale is not colour-blind friendly, so would be hard to interpret for some people. Perhaps use a white to blue scale, with blue indicating stronger winds?

Response: Thank you for the kind reminder. We change the color bar in Fig. 6a/b and line colors in Fig. 3 to be color-blind friendly.

Tables S3 and S4: ‘MAC\_Z500’ in tables should be ‘MCA\_Z500’

Response: Thank you. The typos have been corrected.



## References

- IPCC, Field, C.B., Barros, V., Stocker, T.F., Qin, D., Dokken, D.J., Ebi, K.L., Mastrandrea, M.D., Mach, K.J., Plattner, G.-K., Allen, S.K., Tignor, M., and Midgley, P.M. (eds.): Managing the risks of extreme events and disasters to advance climate change adaptation. A special report of working groups I and II of the Intergovernmental Panel on Climate Change. Cambridge University Press, Cambridge, UK, and New York, NY, USA, 582 pp, 2012.
- Lim, Y. K.: The East Atlantic/West Russia (EA/WR) teleconnection in the North Atlantic: climate impact and relation to Rossby wave propagation, *Clim Dynam*, 44, 3211-3222, 2015.
- Liu, Y. Y., Wang, L., Zhou, W., and Chen, W.: Three Eurasian teleconnection patterns: spatial structures, temporal variability, and associated winter climate anomalies, *Clim Dynam*, 42, 2817-2839, 2014.
- Sardeshmukh, P. D., and Hoskins, B. J.: The Generation of Global Rotational Flow by Steady Idealized Tropical Divergence, *J Atmos Sci*, 45, 1228-1251, 1988.
- Screen, J.A., Deser, C., Simmonds, I. and Tomas, R.: Atmospheric impacts of Arctic sea-ice loss, 1979–2009: Separating forced change from atmospheric internal variability, *Clim. Dynam.*, 43, 1-2, 333-344, 2014.
- Simmons, A. J., Wallace, J. M., and Branstator, G. W.: Barotropic Wave-Propagation and Instability, and Atmospheric Teleconnection Patterns, *J Atmos Sci*, 40, 1363-1392, 1983.
- Zou, Y. F., Wang, Y. H., Zhang, Y. Z., and Koo, J. H.: Arctic sea ice, Eurasia snow, and extreme winter haze in China, *Sci Adv*, 3, 2017.

Response to Referee #2:

#### GENERAL COMMENTS

This paper uses sensitivity experiments to increase our knowledge and understanding of the dynamics and teleconnections whereby Arctic sea ice decline could influence pollution and air quality in China. This is a timely study with some interesting diagnostics and analysis. The approach toward the sensitivity experiments, the diagnostics defined, and the quality and quantity of figures and tables is all good.

However, I have a couple of concerns as outlined below.

Response: Thank you very much for your comments and suggestions. We have revised the manuscript accordingly to address your concerns. Please see below our responses in blue to your specific comments.

#### SPECIFIC COMMENTS

I think lines 22 and 32 are not quite correct as they stand. I'd suggest changing "positive correlations with the regional Arctic sea ice decline" to "positive correlations with the regional Arctic sea ice concentrations", and "positive correlation with the declining sea ice" to "positive correlation with sea ice concentrations". My reading of Figure 1 is that the positive correlation between the EU index and sea ice concentrations in R2 (Figure 1b) suggests that the EU index will decrease as sea ice decreases in R2. Then, the positive PPI index in East Asia in the negative phase of the EU (Figure 1d) suggests that this decreasing EU index will lead to increased pollution in East Asia. Therefore, pollution gets worse in East Asia as sea ice declines in R2. Perhaps section 3.1 would be clearer if re-written slightly to emphasize this?

Response: Thank you for the suggestion. We revised the sentence here to "The winter EUI shows positive correlations with regional Arctic sea ice concentrations with the strongest correlation over the East Siberian Sea and Chukchi Sea (Fig. 1b), suggesting a decrease of EUI in winter following the sea ice decline over these regions in preceding months.". We also explicitly state in the next paragraph that "Since the EUI shows a positive correlation with declining sea ice in the Pacific sector of the Arctic, we would expect more severe air stagnation over East Asia coinciding with the decrease of EUI and regional Arctic sea ice."

Please see Section 3.1 in the revised manuscript for details.

My major concern with this paper is with regards to how relevant this key conclusion is to the real world (which will experience SENSall). Figure 1b shows negative correlations in R1 and R3, so declining sea ice in these regions will improve pollution in East Asia, cancelling the impacts of sea ice decline in R2. Indeed, Tables S3 and S4 indicate no significant difference in PPI between the CTRL and SENSall experiments. This concern, that the substantial conclusions in this paper are all based on SENSr2 which may not be a realistic scenario, will need to be addressed.

Response: Thank you for the helpful discussion. We agree with you that the climate system in the real world has much more complex interactive processes among different components than in climate models, and it's still difficult to find a consensus on the potential influence of Arctic warming and sea ice decline on midlatitude extreme weather due to relatively low signal-to-noise ratios (Cohen et al., 2020). Resonating with a common aphorism that "all models are wrong, but some are useful", we interpret our modeling results from the following perspectives: (1) The key conclusion suggests distinct climate impacts of sea ice loss in different Arctic regions, which is consistent with previous studies (Screen, 2017; Sun et al. 2015, McKenna et al., 2018). Such region-dependent sensitivity along with the associated dynamic process analysis helps to improve understanding of how Arctic warming can affect midlatitude weather and climate extremes. Previously, Barnes and Screen (2015) discussed a similar topic by framing their inquiries around three different questions: "Can Arctic warming influence the midlatitude jet-stream? (Can it?) Has Arctic warming significantly influenced the midlatitude jet-stream? (Has it?) Will Arctic warming significantly influence the midlatitude jet-stream? (Will it?)". They concluded that a growing consensus in the model-based studies that Arctic warming *can* significantly influence the midlatitude circulation does not necessarily imply that it *has* in the past, nor that it *will* in the future (Barnes and Screen, 2015). Their thoughts about these three questions provide insight into the discussion here—that is, our modeling results can be more suitably used to answer the "Can it?" question rather than the "Has it?" one posed in your comment. The answer to the second question is closely related with dynamic processes that actually happened in the real atmosphere, while the answer to the first one is not. Therefore, we can rely on idealized modeling experiments to

isolate specific climate effects of interest to answer the “*Can it?*” question, which is the major motive of this study. It’s noted that the real world does not experience the SENSall experiment since the sea surface temperatures and sea ice concentrations in the WACCM model experiments are prescribed without the two-way air-sea interactions. These processes are considered by the fully coupled CMIP6 model simulations as shown in Section 3.4 and Fig.7, which also help to answer the “*Can it?*” and “*Will it?*” questions rather than “*Has it?*”.

(2) The sensitivity results identify key regions of interest to improve air quality seasonal forecasts. Satellite observations show varying sea ice variability in different years and Arctic regions (Fig. R1/R2). The teleconnection between high latitudes and midlatitudes may be dominated by different dynamic processes associated with changes in subregions of the Arctic from interseasonal to interannual time scales. Previous studies have suggested changing importance of regional sea ice forcing in different months/seasons (Screens, 2017), which is also evident in our SENSall monthly results (Fig. R3/R4). The proposed teleconnection relationship among regional Arctic sea ice, EUI, and ECP\_PPI is most prominent in December, with negatively shifted EUI (Fig. R4a) and more positive extremes of ECP\_PPI (Fig. R4d) in this month than others. Figure S10 in the Supplement shows similar intra-seasonal variations in SENSr2 atmosphere responses, with more negative EU patterns emerging in early winter than in late winter. However, the studied R2 regional forcing-response relationship can be overwhelmed by other Arctic regional forcings or other climate factors such as tropical forcings in the real atmosphere. That’s why a consensus on the climate impact of Arctic warming is difficult to achieve. Our idealized modeling experiments and dynamic diagnosis provide a plausible pathway of how regional Arctic change can affect midlatitude air stagnation weather extremes, while extended and fully coupled experiments are suggested in the discussion part to further investigate the relative importance of different pathways and their roles in the real atmosphere.

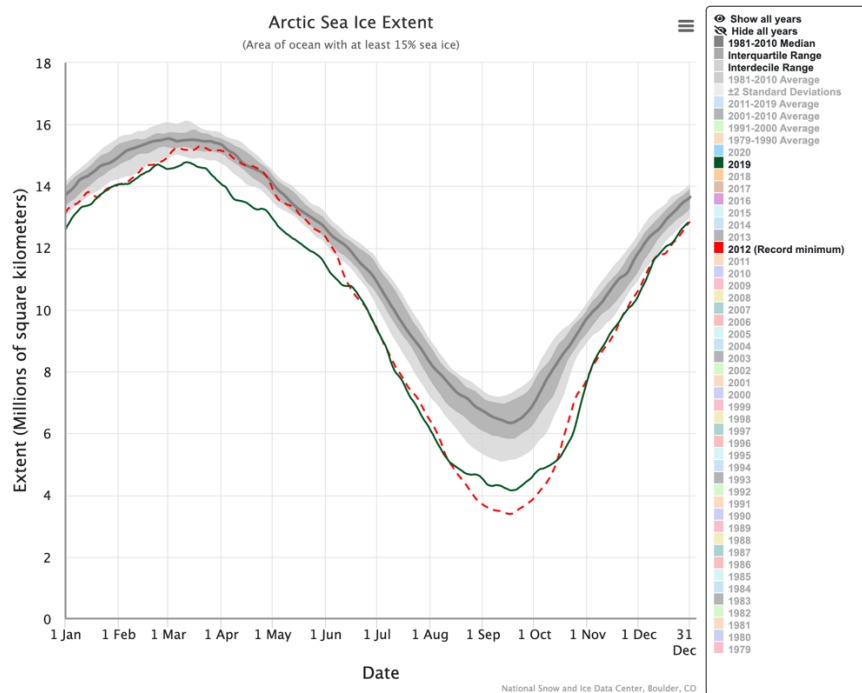


Figure R1: Comparison of Arctic sea ice extent time series between 2012 and 2019 (adapted from the NSIDC website at <https://nsidc.org/arcticseaicenews/charctic-interactive-sea-ice-graph/>; last access: 14 February, 2020).

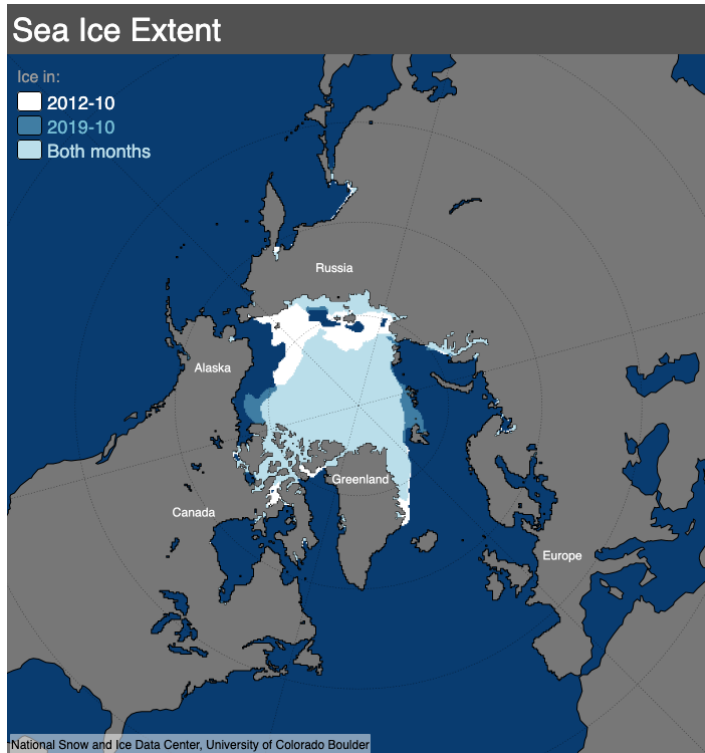


Figure R2: Comparison of Arctic sea ice extent spatial distributions between 2012/10 and 2019/10 (adapted from the NSIDC website at <http://nsidc.org/arcticseaicenews/sea-ice-comparison-tool/>; last access: 14 February, 2020)

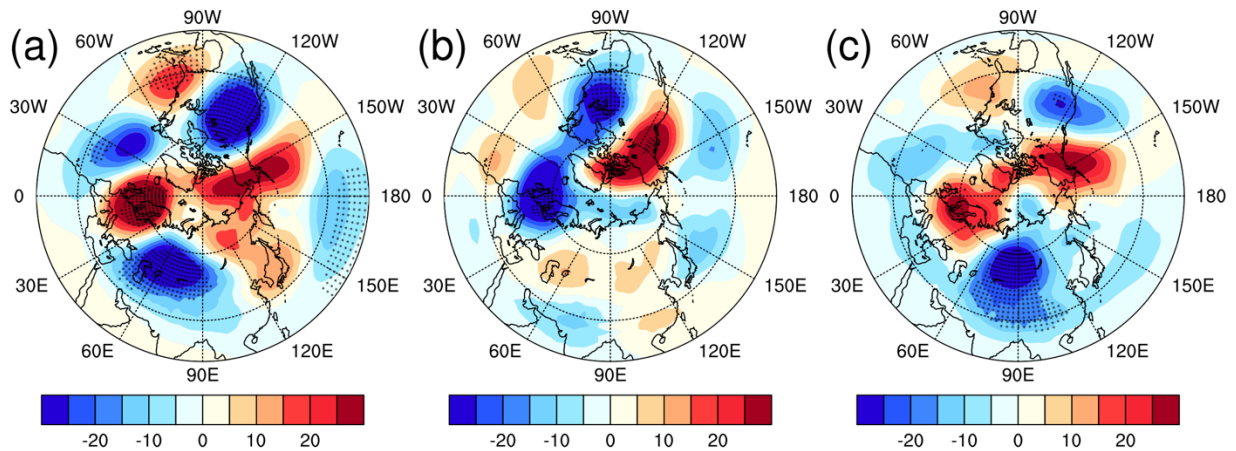


Figure R3: SENSall geopotential height anomalies at 500 hPa in (a) December; (b) January; (c) February. The stipples denote the 0.05 significance level.

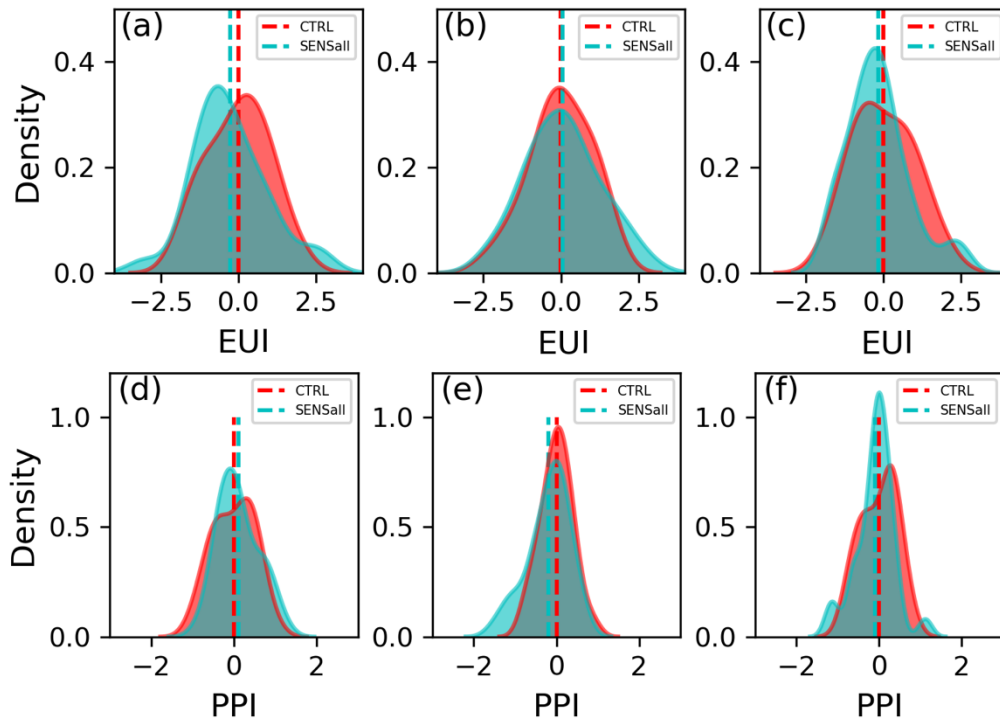


Figure R4: Comparison of KDE-based distribution density estimates in CTRL and SENSall for (a) EUI in December; (b) EUI in January; (c) EUI in February; (d) ECP\_PPI in December; (e) ECP\_PPI in January; (f) ECP\_PPI in February; The dash lines denote ensemble averages.

Checking of the English grammar and language throughout the manuscript is required. To give a couple of examples: on page 2 line 4 "environmental stressors" should be "environmental stresses", and on page 7 line 21 "are the same with these" should be "are the same as those".

Response: We have now checked the English language throughout the manuscript and made a few more corrections.

The description of some of the calculations and diagnostics used in the paper could be slightly clearer. For example, in section 2.3, which "statistical functions in Python" were used, and what is meant by "proper distributions"? Also, please expand on the definitions of WSI and ATGI to make clearer exactly how these are calculated.

Response: Thank you for the suggestion. We have added more detailed descriptions for the calculations and definitions. For example, the Python statistical functions include "normaltest" and "shapiro" for normality tests in Table S2 and Fig. S2/S3, "skew" and "kurtosis" to compute skewness and kurtosis of data sets in Table S2, "norm.fit" to fit normal distributions if the data samples pass normality tests (Fig. S2/S3), or "gumbel\_r.fit"/"gumbel\_l.fit" to fit right-skewed/left-skewed Gumbel distributions if not (Fig.S2/S3), etc. These explanations are added in Section 2.3 of the revised manuscript.

We also added the descriptions of WSI and ATGI in lines 34-37 of page 3:

"WSI was standardized by subtracting time-averaged climatological mean of near-surface wind speed over the 1981-2010 period from the monthly values at each grid cell and then dividing by its standard deviations in the same period. ATGI was the standardized potential temperature gradient field between 925 and 1000 hPa using the same method. These two indices are used to reflect horizontal and vertical dispersions of near-surface air pollutants, respectively."



We revised the manuscript extensively to address these problems. Please see our revised manuscript with tracked changes for details.

#### MINOR COMMENTS AND TYPOGRAPHICAL ERRORS

Page 3, line 32: Person should be Pearson.

Response: Thank you. We corrected the typo here.

Page 5: Perhaps change "Fig. 1" to "Fig. 1a" on line 28, and then add reference to "Fig. 1b" on line 31.

Response: Thank you. We added the specific references in the revised manuscript.

Page 10, line 6: "( et al." should be "(et al."

Response: Thank you. It's corrected.

## References

- Barnes, E. A., and Screen, J. A.: The impact of Arctic warming on the midlatitude jet-stream: Can it? Has it? Will it?, *WIREs Climate Change*, 6, 277-286, [10.1002/wcc.337](https://doi.org/10.1002/wcc.337), 2015.
- Cohen, J., Zhang, X., Francis, J. et al.: Divergent consensus on Arctic amplification influence on midlatitude severe winter weather, *Nat. Clim. Chang.*, <https://doi.org/10.1038/s41558-019-0662-y>, 10, 20–29, 2020.
- Screen, J. A.: Simulated atmospheric response to regional and pan-Arctic sea ice loss, *J. Climate*, 30, 3945-3962, 2017.
- Sun, L., Deser, C., and Tomas, R.A.: Mechanisms of stratospheric and tropospheric circulation response to projected Arctic sea ice loss, *J. Climate*, 28, 7824-7845, DOI: [10.1175/JCLI-D-15-0169.1](https://doi.org/10.1175/JCLI-D-15-0169.1), 2015.
- McKenna, C. M., Bracegirdle, T. J., Shuckburgh, E. F., Haynes, P. H., Joshi, M. M.: Arctic sea-ice loss in different regions leads to contrasting Northern Hemisphere impacts, *Geophys. Res. Lett.*, <https://doi.org/10.1002/2017GL076433>, 2018.

# Atmospheric teleconnection processes linking winter air stagnation and haze extremes in China with regional Arctic sea ice decline

Yufei Zou<sup>1</sup>, Yuhang Wang<sup>2</sup>, Zuowei Xie<sup>3</sup>, Hailong Wang<sup>1</sup>, Philip J. Rasch<sup>1</sup>

<sup>1</sup>Atmospheric Sciences and Global Change Division, Pacific Northwest National Laboratory, Richland, WA 99354, USA

<sup>2</sup>School of Earth and Atmospheric Sciences, Georgia Institute of Technology, Atlanta, GA 30332, USA

<sup>3</sup>International Center for Climate and Environment Sciences, Institute of Atmospheric Physics, Chinese Academy of Sciences, Beijing, 100029, China

*Correspondence:* Yufei Zou (yufei.zou@pnnl.gov) and Yuhang Wang (yuhang.wang@eas.gatech.edu)

**Abstract.** Recent studies suggested significant impacts of boreal cryosphere changes on wintertime air stagnation and haze pollution extremes in China. However, the underlying ~~meechanism~~mechanisms of such a teleconnection relationship remains unclear. Here we ~~used~~use the Whole Atmosphere Community Climate Model (WACCM) to investigate dynamic processes leading to atmospheric circulation and air stagnation responses to Arctic sea ice changes. We ~~conducted~~conduct four climate sensitivity experiments by perturbing sea ice concentrations (SIC) and corresponding sea surface temperature (SST) in autumn and early winter over the whole Arctic and three sub-regions in the climate model. The results indicate ~~different~~distinct responses in ~~the general~~circulation patterns and regional ventilation to the region-specific Arctic changes, with the largest increase of both the probability (by ~~120~~132%) and the intensity (by ~~32~~30%) of monthly air stagnation ~~extreme events~~extremes being found in the experiment driven by SIC and SST changes over the Pacific sector of the Arctic (the East Siberian and Chukchi Seas). The increased air stagnation ~~extreme events~~extremes are mainly driven by an amplified ~~hemispheric~~planetary-scale atmospheric teleconnection pattern that resembles the negative phase of the Eurasian (EU) pattern. Dynamical diagnostics suggest that convergence of transient eddy forcing in the vicinity of Scandinavia in winter is largely responsible for the amplification of the teleconnection pattern. Transient eddy vorticity fluxes dominate the transient eddy forcing and produce a barotropic anticyclonic anomaly near Scandinavia and wave-train propagation across Eurasia to the downstream regions in East Asia. The piecewise potential vorticity inversion analysis reveals that this long-range atmospheric teleconnection of ~~the~~Arctic origin takes place primarily ~~in~~via the middle and upper troposphere. The anomalous ridge over East Asia in the middle and upper troposphere worsens regional ventilation conditions by weakening monsoon northwesterlies and enhancing temperature ~~inversion~~inversions near the surface, leading to more and stronger air stagnation and pollution extremes over eastern China in winter. Ensemble projections based on ~~the~~state-of-the-art climate models in the Coupled Model Intercomparison Project Phase 6 (CMIP6) corroborate this teleconnection relationship between high-latitude environmental changes and middle-latitude weather extremes, though the tendency and magnitude vary considerably among each participating model.

## 1 Introduction

The severe ~~haze~~air pollution ~~over the East~~problem in China ~~Plains (ECP) in recent boreal winter~~ has drawn broad attention because of its profound public health (Kan et al., 2012), socioeconomic (Xie et al., 2016), and climatic impacts (Li et al., 2016). In response to an increasing health burden and social costs caused by these environmental ~~stressors, the Chinese government~~stresses, China has prioritized environment protection ~~to address the urgent public health needs (by implementing a very stringent air pollution control policy (the State Council of China, 2013)-) and~~

achieved great success with gradually decreasing annual mean fine particle (PM<sub>2.5</sub>; particulate matter with aerodynamic diameters of 2.5 micrometers or less) concentrations in recent years (Zhang et al., 2019). However, severe haze pollution associated with PM<sub>2.5</sub> and PM<sub>10</sub> (particulate matter with aerodynamic diameters of 10 micrometers or less) in boreal winter still makes clean air a great challenge for China, especially over the East China Plains (ECP) area (Song et al., 2017). Many studies have investigated possible causes of China's haze pollution from various perspectives—the possible causes of the severe haze pollution, ranging from: massive primary pollution emissions (Liu et al., 2016; Sun et al., 2016), rapid secondary pollution formation (Cheng et al., 2016; Huang et al., 2014; Guo et al., 2014; Wang et al., 2016), unfavorable regional circulation features (Jia et al., 2015; Niu et al., 2010; Yin and Wang, 2017), and positive aerosol-weather feedback effects (Ding et al., 2016; Lou et al., 2019; Zhang et al., 2018; Zhong et al., 2018; Lou et al., 2019).) have all been identified as contributing factors. An et al. (2019) provides a recent comprehensive review of the severe haze problems in China and emphasized the synergistic effect of all synergy among these contributing features-factors.

It has also been reported that climate change plays an important role in generating conducive meteorological conditions for the favorable formation and unfavorable ventilation for air pollution pollutants in China and many other regions (Cai et al., 2017; Dawson et al., 2014; Hong et al., 2019; Horton et al., 2014; Wang and Chen, 2016). Several possible climate factors have been investigated for their effects on winter haze pollution in China, including changes in: 1) Arctic sea ice (Wang et al., 2015; Zou et al., 2017); 2) Eurasian snow cover (Yin and Wang, 2018; Zou et al., 2017); 3) El Niño–Southern Oscillation (ENSO; Chang et al., 2016; Sun et al., 2018; Zhao et al., 2018; Zhang et al., 2019); 4) Pacific Decadal Oscillation (PDO; Zhao et al., 2016); and 5) the northwestern Pacific sea surface temperature (SST; Pei et al., 2018). In these studies, researchers mainly focused on the relationships of various climate factors with pollution-related weather conditions such as the intensity of East Asia winter monsoon (EAWM), planetary boundary layer height, precipitation, and circulation patterns that correlated with winter haze pollution in China. The data analysis results were further corroborated by modeling studies (Zhao et al., 2016; Zhao et al., 2018; Zhang et al., 2019; Zou et al., 2017). However, a clear understanding of key dynamic processes linking complex meteorological changes to critical climate factors was still missing, which is necessary to establish a robust causal relationship between remote climate drivers and local atmospheric responses because a good correlation does not necessarily imply causation. Other studies have examined future projections of future air stagnation and pollution conditions based on the Coupled Model Intercomparison Project Phase 5 (CMIP5) high emission scenario (RCP8.5) data (Taylor et al., 2012) different climate scenarios and ended up with contradictory conclusions over the eastern China region (Cai et al., 2017; Hong et al., 2019; Horton et al., 2014), which further highlights the importance of physical process-based analysis of modeling results.

Given the increasing evidence of the profound influence of that climate change—especially that occurring in high-latitude regions—may have an influence on middle-latitude circulation and weather extremes (Cohen et al., 2014; IPCC, 2019), it is imperative to identify the key atmospheric processes driving the circulation responses and to understand the underlying physical mechanisms. Therefore, here we have re-analyzed the particular linkage between Arctic sea ice change for specific extreme weather events. Several possible dynamic pathways linking Arctic warming to midlatitude weather extremes have been proposed and investigated in the past few years (Barnes and Screen, 2015; Overland et al., 2016). However, the observational data and modeling results are sometimes contradictory and are open to different interpretations (Cohen et al., 2020). Therefore, here we revisit the particular linkage between Arctic sea ice and wintertime air stagnation in China identified by our previous study (Zou et al., 2017) and elucidated a teleconnection mechanism based on new climate model sensitivity experiments and dynamic diagnoses. We describe the analytical methods and datasets in Sect. 2 and analysis of model results in Sect. 3, which is followed by discussion and conclusions in Sect. 4.

## 2 Analysis methods and datasets

### 2.1 Observation and reanalysis data

We collected monthly gridded Arctic sea ice concentration (SIC) and sea surface temperature (SST) data for 1950–2018 were collected from the Met Office Hadley Centre (HadISST; Rayner et al., 2003) for statistical analysis and comparison with numerical simulation experiments results. We conducted trend analysis for Arctic sea ice changes and investigated the statistical correlation between these changes and key atmospheric

circulation patterns of interest. The National Centers for Environmental Prediction and National Center of Atmospheric Research (NCEP/NCAR) reanalysis data (Kalnay et al., 1996) was used to calculate indices of a hemispheric-scale Eurasian (EU) pattern (Wallace and Gutzler, 1981) and a regional circulation pattern (MCA\_Z500) over East Asia in the 500 hPa geopotential height field (Z500) (Fig. S1 in the Supplement). ~~The latter pattern was determined using a Maximum Covariance Analysis (MCA) method (Wilks, 2011) as in our previous study (Zou et al., 2017).~~ We focused on these two circulation patterns at different spatial scales given their considerable impacts on winter synoptic weather (Liu et al., 2014; Wang and Zhang, 2015) and regional haze pollution (Li et al., 2019) in China. ~~We also used the NCEP/NCAR reanalysis data to calculate air in China (Li et al., 2019).~~ ~~pollution potential index (PPI) as a synthetic meteorological proxy for describing regional air stagnation severity (Zou et al., 2017).~~ We followed the definition of the EU index (EUI) in Wallace and Gutzler (1981) and calculated the EU index in winter (December-January-February; DJF) from 1951 to 2019 (years are aligned with January of the winter season in this work),

$$EUI = -\frac{1}{4}Z^*(55^\circ N, 20^\circ E) + \frac{1}{2}Z^*(55^\circ N, 75^\circ E) - \frac{1}{4}Z^*(40^\circ N, 145^\circ E) \quad , \quad (1)$$

where  $Z^*$  denotes the normalized monthly mean geopotential height anomalies at 500 hPa using the 1981-2010 average as the climatology. We then regressed the 500 hPa geopotential height anomalies onto this index to get the EU spatial pattern (Fig. ~~1c/d~~), which resembles those reported in Liu et al. (2014), Wallace and Gutzler (1981), and Wang and Zhang (2015) quite well.

We then ~~used the NCEP/NCAR reanalysis data to calculate~~ gridded pollution potential index (PPI) as a synthetic meteorological proxy for describing regional air stagnation severity (Zou et al., 2017). ~~calculated~~ The monthly PPI in winter (DJF) PPI in of 1951–2019 based on ~~was calculated using Eq. (2) as a weighted average of~~ normalized surface wind speed index (WSI) and near surface air temperature gradient index (ATGI) based on the reanalysis data ~~in Eq. (2). We first, WSI was standardized by subtracting time-averaged climatological mean of near-surface wind speed over the 1981-2010 period from the monthly values at each grid cell and then dividing by its standard deviations in the same period. ATGI was the standardized potential temperature gradient field between 925 hPa and 1000 hPa for each grid cell by subtracting their time-averaged values over 1981-2010 using the same method. These two indices are used to reflect horizontal and dividing by the standard deviations in the same period, vertical dispersions of near-surface air pollutants, respectively.~~ We then estimated grid-scale PPI by weighted averaging wind speed index (WSI) and air temperature gradient index (ATGI),

$$PPI = \frac{r_1 \times WSI + r_2 \times ATGI}{|r_1| + |r_2|} \quad , \quad (2)$$

where  $r_1$  and  $r_2$  are the ~~Person~~ Pearson correlation coefficients of WSI ( $r_1 = -0.73$ ) and ATGI ( $r_2 = 0.70$ ) with in situ PM<sub>10</sub> observations over the ECP area (Zou et al., 2017). ~~The regional~~ Regional averaged ECP\_PPI was estimated by averaging grid-scale PPI over the ECP area (112° E to 122° E, 30° N to 41° N).

Lastly, we applied the ~~MCA method~~ Maximum Covariance Analysis (MCA) method (Wilks, 2011) as in our previous study (Zou et al., 2017) to the Z500 and PPI fields and identified the regional MCA\_Z500 pattern that had the largest covariance with PPI changes in ECP. The MCA analysis performs a singular value decomposition of the covariance matrix of the selected two variables and generates a series of coupled modes in space and time dimensions for both variables (Wilks, 2011). We chose the first couple of modes in the Z500 and PPI fields as the MCA\_Z500 and MCA\_PPI patterns that show the largest covariance with each other ( $r=0.65$ ; Fig. ~~S1S1b~~ in the Supplement). The MCA\_Z500 pattern resembles a regional manifestation of the ~~hemispheric~~ planetary-scale EU pattern (in negative phase) with a good correlation between these two indices ( $r=-0.67$ ; Fig. ~~S1S1b~~ in the Supplement). However, it's worth noting that this regional MCA\_Z500 pattern can also be excited by other large-scale teleconnection processes such as the East Atlantic pattern or the East Atlantic/Western Russia pattern associated with both natural variability and perturbed atmospheric ~~Rossby~~ wave activity- (Lim, 2015; Simmons et al., 1983). These variables ~~were~~ are assessed as metrics of circulation and ventilation responses to climate forcing in the following sections.

## 2.2 Climate models and numerical sensitivity experiments

This study uses the high-top Whole Atmosphere Community Climate Model (WACCM) version 5 (Marsh et al., 2013) ~~under~~ within the common numerical framework of the NCAR Community Earth System Model (CESM) used for climate sensitivity experiments. WACCM is a comprehensive atmospheric model with a well-resolved stratosphere of 70 vertical layers spanning the surface to the thermosphere (~0.001 hPa) at a horizontal resolution of



1.9° (latitude) × 2.5° (longitude). We conducted 30-year simulations (with an additional unanalyzed 1-year period for the control run as spin-up) as the control (CTRL) run with annually repeating prescribed climatological (1981-2010 average) Arctic SIC and SST from the Met Office Hadley Centre (Rayner et al., 2003) (Table 1). We then performed four climate sensitivity experiments by perturbing SIC and SST in different Arctic regions to investigate the climate sensitivity to regional Arctic sea ice changes and associated local ocean warming (Screen et al., 2013).

The spatial distribution of correlation coefficients between SIC and EU indices (Fig. 1b) ~~indicated~~ ~~reveals~~ varying climate sensitivity relationships between regional sea ice changes and circulation responses as suggested by previous studies (Screen, 2017; Sun et al., 2015; McKenna et al., 2018). To test this region-specific climate sensitivity, we first perturbed SIC and SST in the whole Arctic region to evaluate their comprehensive climate effects, and then divided the whole Arctic region into three sub-regions (R1-R3; Fig. 1b) and perturbed regional SIC and SST in three region-specific numerical experiments (Table 1). Specifically, we branched an 8-month simulation from each July of the CTRL run with observed SIC/SST data in autumn and early winter (August-November) of 2012 over the whole Arctic in the first sensitivity experiment (SENSall). We chose 2012 because it ~~has~~ ~~had~~ the lowest level of Arctic sea ice concentrations throughout the satellite era of the last four decades (NSIDC/NASA, 2019) and ~~thus~~ provides the strongest sea-ice ~~perturbation~~ ~~forcing~~ to the climate system. We only changed the surface boundary conditions (SIC/SST) at ~~these~~ modeling grid cells with SIC anomalies larger than 10% to focus on the Arctic regions with the most significant changes. We then added three region-specific sensitivity experiments (SENSr1/r2/r3) by perturbing regional SIC and SST in R1-R3 regions (R1: 30° E to 150° E, 70° N to 85° N; R2: 150° E to 145° W, 60° N to 85° N; R3: 145° W to 30° W, 50° N to 85° N; Fig. 1b) ~~),~~ ~~respectively,~~ following the same perturbation method in SENSall.

We analyzed the ~~continuous~~ ~~consecutive~~ December-January-February ~~monthly~~ data at the end of each sensitivity simulation to examine the seasonal impact of Arctic sea ice changes in comparison with observation and reanalysis data. The simulated EU/MCA\_Z500 circulation indices were estimated by projecting modeling differences (SENSx-CTRL, x=all/r1/r2/r3) onto the reanalysis-based EU/MCA\_Z500 patterns, and the ECP\_PPI indices in the model were calculated following the same method of the reanalysis one by using the CTRL ensemble mean as the climatology.

Since the default 2000-based emission inventory (Lamarque et al., 2010) in WACCM was prepared for the Fifth Assessment Report of the Intergovernmental Panel on Climate Change (IPCC AR5) and is low biased over China, we updated the anthropogenic emission inventory ~~in~~ ~~for~~ China by replacing the default one with the 2010-based multi-resolution emission inventory for China (MEIC; Li et al., 2017). The MEIC-MIX inventory was developed for the years 2008 and 2010 and has been widely used for air pollution simulation and health impact assessment studies in China (Geng et al., 2017; Zhang et al., 2017). It is worth noting that the main objective of this study is not to reproduce severe haze pollution extremes in China, but to understand how regional atmosphere and pollution conditions respond to the key climate drivers in the high latitudes. Therefore, we only focused on the relative changes of PPI and surface PM<sub>2.5</sub> concentrations between SENS and CTRL experiments and investigated dynamic processes associated with these changes in our following analysis.

Besides the CESM-WACCM model used in the sensitivity experiments, we also analyzed ~~modeling~~ results from other state-of-the-art climate models in the latest CMIP6 project to examine the teleconnection relationship between Arctic sea ice and regional air stagnation in China. Table S1 in the Supplement lists the 8 CMIP6 models with the same experiment and variant ID (r1i1p1f1) used for historical simulations and future projections of the Arctic sea ice extent (SIE) and ECP\_PPI time series. SIE is a measurement of the ocean area where sea ice concentrations exceed 15% (NSIDC, 2019). We analyzed historical simulations (1950-2014; Eying et al., 2016) and future projections (2015-2100) of the Shared Socioeconomic Pathway under a high greenhouse gas emission scenario (SSP5-8.5; O'Neill et al., 2016) by each model to maintain consistency with previous studies (Cai et al., 2017; Horton et al., 2014). We then calculated time series of regional averaged Arctic SIE and ECP\_PPI in each CMIP6 model to estimate ensemble means and standard deviations of these variables. The estimation of the SIE relative changes and ECP\_PPI indices in CMIP6 followed the same method of the observation- and reanalysis-based ones by using 1981-2010 historical runs as the climatology. The whole 150-year CMIP6 time series ~~of the 150 years were~~ ~~was~~ equally divided into three time periods (P1-P3) to evaluate regional air stagnation conditions under different Arctic sea ice forcing.

## 2.3 Statistical analysis methods

We examined long-term linear trends of observed SIC in each grid cell in Fig. 1a using the Mann-Kendall test, which is a non-parametric (i.e., distribution free) method that is based on the relative ranking of data values. After trend detection, we estimated the Pearson correlation between the gridded sea ice variations and the EU index. To evaluate the circulation impact on regional ventilation, we conducted composite analysis of gridded PPIs over the middle latitude regions (Fig. 1b) and examined their statistical significance using the two-sided Student's t-test. The t-test was also used to evaluate statistical significance of surface heat flux changes and atmospheric responses in the modeling results, such as the ensemble mean differences of atmospheric variables between the WACCM SENS and CTRL experiments.

To further evaluate climate modeling sensitivity modeling results, we used statistical functions in the Python (<https://docs.scipy.org/doc/scipy/reference/stats.html>) SciPy v1.4.1 module (<https://docs.scipy.org/doc/scipy/reference/stats.html>; last access: 24 October, 2019) to evaluate statistical properties of the modeling samples and estimate their cumulative distribution functions (CDFs) and probability density functions (PDFs) following proper distributions. We first examined the statistics of the MCA\_Z500 and ECP\_PPI indices in each experiment in terms of their location, scale, and shape (Table S2), and then conducted the Shapiro-Wilk normality test (Wilks, 2011; the “shapiro” function in SciPy v1.4.1) to examine whether the data conform to normal distributions (Fig. S2 and Fig. S3 in the Supplement). The null hypothesis of the normality test is that the sampling data from each experiment are drawn from a normal distribution. If the p-value is larger than 0.05, we failed to reject the null hypothesis and fitted normal distribution (the “norm.fit” function in SciPy v1.4.1) CDF/PDF curves to the modeling data (30 years  $\times$  3 winter months = 90 samples). Otherwise, we rejected the null hypothesis and chose a proper non-Gaussian distribution (e.g., the “gumble\_r.fit”/“gumble\_l.fit” functions in SciPy v1.4.1 for right-skewed/left-skewed distributions) to fit CDF/PDF curves to the data. Table S2 shows these statistical properties and test results of each experiment, which suggests that the data in most experiments conform to normal distributions except MCA\_Z500 in SENSall and MCA\_Z500/ECP\_PPI in SENSr2. The statistics and histograms of the SENSall MCA\_Z500 indices suggest a skew distribution to the left, while these those of the SENSr2 MCA\_Z500/ECP\_PPI indices suggest a skew distribution to the right. Therefore, we fitted a left-skewed Gumbel distribution to the SENSall MCA\_Z500 data and a right-skewed Gumbel distribution to the SENSr2 data, respectively. The goodness-of-fit results are shown in the Q-Q plots of Fig. S2 and Fig. S3 in the Supplement. After distribution fitting, we chose the 95<sup>th</sup> percentiles of the MCA\_Z500 and ECP\_PPI indices in CTRL as the thresholds of positive extremes and estimated the probability of extreme events positive extremes in the four SENS experiments based on their fitted CDF curves (i.e.,  $P_{PPI_{SENS} \geq PPI_{CTRL}^{95th}}$ ). The average intensity of positive extreme values in each experiment was estimated by weighted averaging these weighting values with their probabilities as weights. The fitted CDFs for all the WACCM experiments are shown in Fig. 3 and discussed below. For CMIP6 data, we used the same approach to fit CDF curves for each modeling and the reanalysis data in different time periods. The CDFs for three time periods over 1950-2000 (P1), 2001-2050 (P2), and 2051-2100 (P3) are shown in Fig. 7 and discussed later near that figure. The P1 time period over 1951-2000 was chosen as the reference period for the NCEP reanalysis and CMIP6 modeling data. The thresholds of positive extremes in the reanalysis and CMIP6 models were defined as the 95<sup>th</sup> percentiles of ECP\_PPI values in this reference time period, which were then used to evaluate probability changes of extreme events positive extremes in the other two periods (i.e.,  $P_{PPI_{P2/3} \geq PPI_{P1}^{95th}}$ ).

Such extreme value analyses provide an alternative perspective in addition to the traditional ensemble mean statistics with statistical analysis, lending a more comprehensive understanding of atmospheric responses to climate forcing based on full distribution curves. A special report of the Intergovernmental Panel on Climate Change (IPCC, 2012) focusing on the risks of climate extreme events proposed discussed three kinds of responses including “shifted mean”, “increased variability”, and “changed symmetry” in climate variable distributions to climate change. These distinct responses demonstrate that changes in extremes can be linked to changes in the mean, variance, and shape of probability distributions, or all of these (IPCC, 2012). We followed this analysis framework to examine statistical distribution changes in regional circulation (MCA\_Z500) and ventilation (ECP\_PPI) with consideration of both natural variability and perturbation-induced responses in our climate sensitivity experiments. The uncertainty of the extreme probabilities and intensities in each experiment was evaluated estimated using the 95% percentile ranges (i.e., values between the 2.5<sup>th</sup> percentile to 97.5<sup>th</sup> percentile) via a bootstrap method by resampling the model simulated samples 5000 with replacement (10000 times) and re-estimating those statistics based on the repeatedly fitted CDFs (Tables S3 and S4 in the Supplement).

## 2.4 Diagnostics of atmospheric dynamics

To understand the atmospheric ~~pathway~~ pathways from the Arctic sea ice forcing to regional circulation responses, we employed multiple dynamic diagnostic tools to investigate storm-track characteristics and local interactions between transient eddy forcing and the time-mean flow. The properties of transient eddies were depicted by eddy kinetic energy (EKE) in Eq. (3) and the horizontal components of extended Eliassen-Palm vectors (**E** vectors) in Eq. (4) given by ~~Hoskins et al. (1983)~~ Trenberth (1986),

$$EKE = \frac{1}{2} (\overline{u'^2} + \overline{v'^2}), \quad (3)$$

$$\mathbf{E} \text{ vector} = \frac{1}{2} (\overline{v'^2} - \overline{u'^2}) \mathbf{i} - \overline{u'v'} \mathbf{j}, \quad (4)$$

where  $u$  and  $v$  are the daily zonal and meridional wind components, respectively. The prime denotes the 2–8-day band-pass-filtered quantities and the overbar denotes ~~time~~temporal averaging over a month.

The direction of **E** vectors approximately points to the wave energy propagation relative to the local time-mean flow, while the divergence and curl of **E** vectors indicate eddy-induced acceleration of local mean zonal and meridional winds (~~Hoskins et al., 1983~~; Trenberth, 1986).

We then illustrated transient eddy feedback to the quasi-stationary flow by eddy-induced geopotential height tendencies due to the convergence and divergence of transient eddy vorticity and heat fluxes (Lau and Holopainen, 1984; Lau and Nath, 1991),

$$\left\{ \frac{1}{f} \nabla^2 + f \frac{\partial}{\partial p} \left( \frac{1}{\sigma} \frac{\partial}{\partial p} \right) \right\} \left( \frac{\partial \phi}{\partial t} \right) = D^V + D^H, \text{ where } D^V = -\nabla \cdot (\overline{V' \zeta'}) \text{ and } D^H = f \frac{\partial}{\partial p} \left( \frac{\overline{v' \theta'}}{s} \right). \quad (5)$$

In Eq. (5),  $D^V$  and  $D^H$  are the eddy forcing due to heat and vorticity fluxes, respectively.  $f$  is the Coriolis parameter,  $\phi = gz$  is geopotential,  $\sigma = -\left(\frac{\alpha}{\theta}\right) \left(\frac{\partial \theta}{\partial p}\right)$  is static stability,  $\alpha$  is specific volume,  $\theta$  is potential temperature with  $S = -\frac{\partial \theta}{\partial p}$ ,  $V$  is horizontal wind, and  $\zeta$  is relative vorticity. Here the prime and overbar are the same with ~~these~~those in Eqs. (3) and (4). By inverting the eddy forcing terms  $D^V$  and  $D^H$  on its right-hand side separately and solving the equation, we could distinguish ~~each effect~~ independent effects of vorticity and heat fluxes induced by transient eddies on the corresponding height tendencies  $Z_t^V$  and  $Z_t^H$ . The net tendency associated with the combination of  $D^V$  and  $D^H$  is denoted as  $Z_t^{V+H}$ .

Moreover, we used the phase-independent 3-dimensional wave activity flux (WAF; Takaya and Nakamura, 2001) based on the monthly averaged reanalysis and modeling data to diagnose zonal and vertical propagation of locally forced wave packet induced by quasi-geostrophic (QG) eddy disturbances embedded in a zonally varying basic flow,

$$\mathbf{W} = \frac{p \cos \phi}{2|U|} \begin{bmatrix} \frac{u}{a^2 \cos^2 \phi} \left[ \left( \frac{\partial \psi'}{\partial \lambda} \right)^2 - \psi' \frac{\partial^2 \psi'}{\partial \lambda^2} \right] + \frac{v}{a^2 \cos \phi} \left[ \frac{\partial \psi'}{\partial \lambda} \frac{\partial \psi'}{\partial \phi} - \psi' \frac{\partial^2 \psi'}{\partial \lambda \partial \phi} \right] \\ \frac{u}{a^2 \cos^2 \phi} \left[ \frac{\partial \psi'}{\partial \lambda} \frac{\partial \psi'}{\partial \phi} - \psi' \frac{\partial^2 \psi'}{\partial \lambda \partial \phi} \right] + \frac{v}{a^2} \left[ \left( \frac{\partial \psi'}{\partial \phi} \right)^2 - \psi' \frac{\partial^2 \psi'}{\partial \phi^2} \right] \\ \frac{f_0^2}{N^2} \left\{ \frac{u}{a \cos \phi} \left[ \frac{\partial \psi'}{\partial \lambda} \frac{\partial \psi'}{\partial z} - \psi' \frac{\partial^2 \psi'}{\partial \lambda \partial z} \right] + \frac{v}{a} \left[ \frac{\partial \psi'}{\partial \lambda} \frac{\partial \psi'}{\partial z} - \psi' \frac{\partial^2 \psi'}{\partial \lambda \partial z} \right] \right\} \end{bmatrix} + \mathbf{C}_U M. \quad (6)$$

Here  $u$  and  $v$  are the zonal and meridional wind components, respectively.  $\mathbf{U} = (u, v, 0)^T$  is a steady zonally inhomogeneous basic flow.  $p = (\text{pressure}/1000 \text{ hPa})$  is normalized pressure,  $\psi'$  is a ~~perturbation~~ streamfunction ~~perturbation relative to the climatological mean~~,  $(\phi, \lambda)$  are latitude and longitude,  $a$  is the earth's radius,  $N^2 = (R_a p^k / H) (\partial \theta / \partial z)$  is the squared buoyancy frequency,  $\mathbf{C}_U$  represents the phase propagation in the direction of  $\mathbf{U}$ , and  $M$  can be interpreted as a generalization of small-amplitude pseudo-momentum for QG eddies onto a zonally varying basic flow.

Lastly, we quantified the influence of circulation anomalies at different vertical levels using a piecewise potential vorticity (PV) inversion method (Black and McDaniel, 2004); ~~Xie et al., 2019~~. The PV anomalies were calculated with reanalysis and simulation data for all troposphere pressure levels from 1000 hPa to 100 hPa in Eq. (7),

$$q' = \frac{1}{f} \left[ \frac{1}{(a \cos \phi)^2} \frac{\partial^2}{\partial \lambda^2} + \frac{f}{a^2 \cos \phi} \frac{\partial}{\partial \phi} \left( \frac{\cos \phi}{f} \frac{\partial}{\partial x} \right) + f^2 \frac{\partial}{\partial p} \left( \frac{\partial}{\partial p} \right) \right] \Phi' \quad (7)$$

where  $q$  is the PV,  $\phi$  is the geopotential,  $f$  is the Coriolis parameter, and a prime represents the deviation from the smoothed climatological annual cycle. We then inverted individual PV “pieces” at different levels to evaluate near surface (850 hPa) horizontal wind anomalies related to these PV anomalies. The horizontal anomalous wind field that will be presented in Fig. 6 was derived from the geopotential height field based on geostrophic balance. We partitioned the 1000-100 hPa PV anomalies into the lower-troposphere (1000-850 hPa) and the middle to upper troposphere (700-100 hPa) PV anomalies and compare their impacts on the near surface wind field in Sect. 3.

## 3 Results

### 3.1 Observation- and reanalysis-data based relationships among Arctic sea ice, atmospheric circulation, and boundary-layer ventilation

We first examined the long-term variations of Arctic sea ice in autumn and early winter (August to November, ASON) of the past four decades during the satellite era. Figure 1a shows the strong decreasing trends in the Arctic sea ice extent (SIC), especially in the Eurasian and Pacific sectors such as the northern Barents Sea, Kara Sea, East Siberian Sea, and Chukchi Sea. The winter EU index (EUI) shows positive correlations with the regional Arctic sea ice concentrations with the strongest correlation over the East Siberian Sea and Chukchi Sea (Fig. 1b), suggesting a decrease of EUI in winter following the sea ice decline over these regions in preceding months. The correlation coefficient between EU and regional averaged SIC over these positively correlated R2 grids is 0.38 ( $p=0.02$ ). Positive correlations are also present when the long-term trend in regional sea ice changes is removed, suggesting a consistent relationship between EU variations and sea ice changes in these Arctic regions on shorter (both long-term (interdecadal) and short-term (interannual) time scales.

To evaluate the impact of EU phases on regional ventilation, we conducted composite analysis and compared wintertime boundary-layer PPI differences over the Northern Hemisphere corresponding to different EU phases. In general, PPI and EU show an in-phase relation with high (low) PPI anomalies corresponding to positive (negative) height anomalies in the EU pattern (Fig. 1c, d). Europe and East Asia become two hot-spot regions in the negative EU phase (Fig. 1d), implying significant sensitivity (i.e., lower ventilation capability and higher air pollution potential) in these regions. Since the EUI shows a positive correlation with the declining sea ice in the Pacific sector of the Arctic, we would expect more severe air stagnation to occur in the hot-spot regions over East Asia coinciding with the decrease of EUI and regional Arctic sea ice observed there.

### 3.2 WACCM sensitivity simulations

The statistical analysis suggests a potential linkage between the Arctic sea ice decline and the regional ventilation deterioration through a circulation change in the negative EU phase. We re-evaluated the teleconnection relationship using ensemble WACCM sensitivity experiments (Table 1). Figure 2 shows the mean surface sensible plus latent heat flux changes between the SENSall and CTRL experiments during autumn and winter. Since we perturbed the Arctic SIC and SST in the model surface boundary conditions from August to November, most Arctic regions show significantly increased heat fluxes in autumn and early winter, especially over the Kara Sea, Laptev Sea, East Siberian Sea, and Beaufort Sea (Fig. 2a). The heat flux changes are much weaker in winter with some remnant influence over the Kara Sea (Fig. 2b) due to the strong perturbation in this region. The comparison of monthly variations in regional averaged heat fluxes over the Arctic confirms the much stronger forcing in ASON (seasonal mean heat fluxes increased by  $3.3 \text{ W/m}^2$  or +16% over the Arctic in SENSall) than in DJF (seasonal mean heat fluxes decreased by  $0.17 \text{ W/m}^2$  or -1% over the Arctic in SENSall) (Fig. 2c).

To examine the regional circulation and ventilation responses to these changes in the high latitudes, we fitted the CDF and PDF curves of MCA\_Z500 and ECP\_PPI based on CTRL and SENS modeling monthly results in winter. Figure 3 shows the CDF changes of simulated MCA\_Z500 (Fig. 3a) and ECP\_PPI indices (Fig. 3b) between sensitivity and CTRL experiments. It is clear that both indices show more significant changes in their extreme members than in medians or ensemble means, especially in SENSr2 driven by SIC and SST changes in the Pacific sector of the Arctic (R2 in Fig. 1b). In SENSr2, the occurrence probability of MCA\_Z500 positive extremes increases by 80% from 5.0 to 9%  $\pm$  3% 7.5% (95<sup>th</sup> percentile range: 0.8-16.4%) (Fig. 3a; Table S3 in the



Supplement), while the ECP\_PPI positive extremes increases by ~~120~~132% to  $11\% \pm 3\%$  (95% percentile range: 5.2-18.4%) (Fig. 3b; Table S3 in the Supplement). Meanwhile, the intensity of positive extreme values of ~~both the~~ two indices also increases by 2611% and 3230%, respectively (Table S4 in the Supplement). ~~Such largely~~ The increase in the teleconnection pattern index MCA\_Z500 is less significant than that in the regional air stagnation index ECP\_PPI, suggesting a potential nonlinear relationship between large-scale circulation and regional stagnation. Only SENSr2 shows statistically significant increases of ECP\_PPI in terms of positive extreme probability and intensity, and the significance of such increases is independent from the fitting method being used (i.e., still valid with nonparametric curve fitting). The substantially increased positive extremes in both indices of SENSr2 contribute to the positive responses in the its ensemble means of two indices mean, making SENSr2 the only sensitivity experiment with positive ensemble mean ECP\_PPI- (0.03, not statistically significant). In comparison, other SENS experiments generally show negative ensemble mean ECP\_PPI values due to negatively-left-shifted CDF curves at most percentiles. For instance, both curves in SENSr1 driven by the regional SIC/SST perturbation in the Barents-Kara Seas (R1 in Fig. 1b) show complete shifts toward the left side within the only experiment showing robustly decreased ECP\_PPI at all percentiles in its CDF curve (Fig. 3b), contributing to its negative ensemble means and medians of MCA\_Z500 and ECP\_PPI indices as well as more negative extremes at low quantiles and less positive extremes mean of ECP\_PPI (-0.13) that is statistically significant at high quantiles, suggesting the 0.05 significance level (Table S2 in the supplement). This result implies an overall decrease of air stagnation and increase of improvement of the ECP regional ventilation driven by the SIC and SST changes in this region-the Barents-Kara Seas (R1 in Fig. 1b), while the ventilation responses are more random driven by sea ice loss in other Arctic regions.

The disparate results among the sensitivity experiments highlight distinct climate effects of regional SIC/SST changes as suggested by both statistical analysis in the last section and previous climate modeling studies. Screen (2017) and McKenna et al. (2018) investigated atmospheric responses to regional sea ice loss by perturbing regional SIC and SST or surface temperature. McKenna et al. (2018) focused on the climate impacts of sea ice loss in the Atlantic (the Barents-Kara Seas) and the Pacific sectors (the Chukchi-Bering Seas) of the Arctic, while Screen (2017) conducted more comprehensive investigation by dividing the whole Arctic region into nine sub-regions. These region-specific modeling studies suggested quite different or even opposite effects of regional sea ice forcing on general circulation in the stratosphere and troposphere. However, it is worth noting that they mainly focused on the responses in the stratospheric polar vortex and in the tropospheric Arctic Oscillation (AO) and North Atlantic Oscillation (NAO), which are different from the EU and MCA\_Z500 patterns of interest in this work.

The differences in the MCA\_Z500 and ECP\_PPI responses among the four sensitivity experiments in extreme members and ensemble means also suggest complex relationships between Arctic sea ice loss and mid-latitude weather changes. Two distinct patterns of Asian winter climate responses to Arctic sea ice loss were identified in a previous study (Wu et al., 2015), one (the “Siberian High” pattern) in positive phase associated with the strengthened Siberia High and EAWM systems while the other (the “Asia-Arctic” pattern) in negative phase associated with weakened EAWM and enhanced precipitation in East Asia. Such opposite responses in regional climate and weather systems partly explain the concurrent changes in the two tails of distribution curves in our sensitivity experiments. An IPCC report (IPCC, 2012) demonstrated three kinds of responses in variable probability distributions to climate change, and our ECP\_PPI results in the four SENS experiments agree with the proposed “increased variability”, “shifted mean”, “changed symmetry”, and “increased variability” responses, respectively (see section 2.3 and Table S2 and Fig. S3 in the Supplement for explanations). These distinct responses reflect complex interactions between atmospheric anomalies driven by climate forcing and atmospheric circulation associated with the natural variability. The coupling

Coupling processes among different components of the climate system ~~would~~can compound such complexity by amplifying or dampening signal-to-noise ratios and expanding responsive regions (Deser et al., 2015; Deser et al., 2016). Smith et al. (2017) pointed out the importance of ocean-atmosphere coupling and the background state in modulating atmosphere responses to Arctic sea ice changes. They found that the background state plays a key role in determining the sign of the NAO responses to Arctic sea ice loss via the refraction of planetary waves by the climatological flow (Smith et al., 2017). These findings shed light on the diverse responses in our simulated distributions of MCA\_Z500 and ECP\_PPI because of the varying background flow in each modeling year. It is worth noting that we only changed the surface boundary conditions (SIC/SST) at these model grid cells with sea ice changes larger than 10% and kept other grid cells unperturbed. Because our study design used prescribed ocean data, the ice-ocean-atmosphere coupling is constrained and it might attenuate other atmospheric responses to sea ice changes as discussed in previous studies (Deser et al., 2015; Deser et al., 2016; Smith et al., 2017).

Considering air pollution responses, we found exacerbated haze pollution represented by positive anomalous PM<sub>2.5</sub> surface concentrations in eastern China regions concurrent with the increased ECP\_PPI extreme values in all SENS experiments. The changes in surface PM<sub>2.5</sub> concentration fields correspond well with the PPI changes with the most significant increases in SENSr2 (Fig. S4c in the Supplement) due to the largest number of positive extreme members in this case (Fig. 3b). These positive PPI extremes in SENSr2 are attributed to both reduced surface wind speed and enhanced near surface temperature inversion (Fig. S5 in the Supplement). The agreement between PPI and surface PM<sub>2.5</sub> concentration changes demonstrates the promising capability of PPI for describing regional air stagnation and pollution potentials. Since the cause of increasing extreme events air stagnation extremes is the major concern of this work, we mainly focus on analyzing the dynamic processes contributing to the largest increase of ECP\_PPI extremes in SENSr2 diagnosis in the next section: to understand the following two questions: (1) how does severe air stagnation occur in these SENSr2 extreme members? (2) why are there more and intensified air stagnation extremes in SENSr2?

### 3.3 Diagnosis of dynamic processes

To elucidate the dynamic mechanisms of air stagnation extreme events driven by first question raised in the Arctic sea ice forcing previous section, we examine atmospheric responses anomalies induced by sea ice perturbations in the SENSr2 extreme members from the perspective of wave activity fluxes and transient eddy feedback forcing in winter over the Northern Hemisphere based on the SENSr2 extreme members. We also evaluate climate impacts of the anomalous circulations and teleconnection patterns in these extremes on regional ventilation using the piecewise PV inversion method. We first describe the anomalous geopotential height field in the upper troposphere (250 hPa, Fig. 4a) and sea level pressure anomalies (Fig. 4b), both of which share similar features with strong positive anomalies over the North Pacific and Northern Europe and negative ones over central Siberia. This quasi-barotropic structure over most regions of the Northern Hemisphere agrees with previous findings regarding Arctic sea ice induced atmospheric responses at interseasonal scales (Deser et al., 2010). The geopotential height anomalies in the upper troposphere manifest wave-train patterns with enhanced Rossby wave propagation from the North Pacific to North America and over the Eurasian continent (Fig. 4a). The sea level pressure anomalies exhibit eastward displacements with respect to the upper-troposphere anomalies over Eurasia (Fig. 4b). In particular, the negative sea level pressure anomaly over Siberia extends southeastward to southeastern China, suggesting a weakened Siberia High. In response, anomalous surface southerlies are seen along the coastal region of eastern China that offset the prevalent winter monsoon and thus increase the air stagnation in winter over eastern China.

We then compare the difference of EKE and  $\mathbf{E}$  vectors (section 2.4) between SENSr2 extreme members and CTRL ensemble mean and calculated anomalous 250 hPa geopotential height tendencies driven by transient eddies using Eq. (5). The most prominent features in the anomalous zonal wind and transient eddy fields are zonal positive anomalies over the mid-middle latitudes from the northeastern Pacific to North Africa that are to the south of the upper-troposphere negative height anomalies (Fig. 4c). Meanwhile, both zonal wind and EKE fields feature a moderate dipole around the positive height anomaly. The divergence of  $\mathbf{E}$  vectors is seen from the northeastern Pacific to the North Atlantic, which results in amplifications of zonal winds and a climatology-like pattern of transient eddy feedback forcing with zonally elongated positive height tendencies to the south of negative height tendencies (Fig. 4d). In contrast, the  $\mathbf{E}$  vectors converge over the vicinity of the Scandinavian region (Fig. 4d), suggesting a weakened zonal wind and thereby depress transient eddy activity. Accordingly, significant geopotential height tendencies driven by transient eddy forcing emerge in the upper troposphere, showing pronounced positive anomalies near the Scandinavian region. These tendencies are dominated by transient eddy vorticity forcing rather than transient eddy heat forcing, the latter of which shows opposite but much weaker effects on the upper level geopotential height field (Fig. S6 in the Supplement). Both transient eddy vorticity and heat flux forcing contribute constructively in the lower troposphere (Fig. S6 in the Supplement).

We further compare the simulated atmospheric anomalies relative to the ensemble average of the 30 strongest negative EU years (10 minimums for each Dec/Jan/Feb month) in winter since 1950 in the reanalysis data. Figure 5 shows the horizontal (250 hPa) and vertical structures of wave propagation in reanalysis-based negative EU extremes and SENSr2 extreme members. They show similar features of wave train patterns with (Fig. 5a, d) and model-based SENSr2 extreme members (Fig. 5b, e; hereafter SENSr2<sub>extreme</sub>) and their CTRL counterparts (Fig. 5c, f; hereafter CTRL<sub>counterpart</sub>). The comparison between the last two modeling results shed light



on the question of why more extremes occur in SENSr2 than in CTRL. It's apparent that SENSr2<sub>extreme</sub> shares more similar features of wave train propagation with the reanalysis data than the CTRL<sub>counterpart</sub> does, characterized by two anomalous troughs over the North Atlantic (region A in Fig. 5a, b) and the Siberian (region C in Fig. 5a, b) areas and two anomalous ridges over the Scandinavian Peninsula (region B in Fig. 5a, b) and East Asia (region D in Fig. 5a, b) areas. These wave train patterns exhibit barotropic vertical structures in the troposphere in both cases (Fig. 5e, 5d, c). Unlike the reanalysis members data, the wave train pattern of SENSr2<sub>extreme</sub> shows a westward tilt in the lower troposphere with evident downward energy propagation. To understand why more extreme members occurred in SENSr2 than CTRL, we overlapped CTRL<sub>counterpart</sub> with much weaker wave activity, resulting in disappeared key features along the vertical structure of the corresponding CTRL members (contours in propagation pathway (Fig. 5d) to SENSr2<sub>extreme</sub> members (shading in Fig. 5d) and compared their differences (Fig. 5c, f). Though these CTRL<sub>counterpart</sub> members share the same initial condition and similar with SENSr2<sub>extreme</sub>, they show different vertical structures of wave train patterns with SENSr2<sub>extreme</sub> members in both upstream regions (e.g., the middle and upper lower troposphere over region B) and C), a key difference emerges over the downstream region of East Asia (region D). Meanwhile, the anomalous centers of CTRL<sub>counterpart</sub> members are higher than the SENSr2<sub>extreme</sub> members and the reanalysis counterparts data, which is unfavorable for the lateral Rossby wave propagation to help the formation of the positive height anomalies over East Asia. In contrast to negative to neutral height anomalies in CTRL members, these SENSr2<sub>extreme</sub> members manifest positive anomalies in the middle to upper troposphere over this region. CTRL<sub>counterpart</sub>, SENSr2<sub>extreme</sub> manifests positive anomalies in the middle to upper troposphere over this region (Fig. 5e). To highlight such difference between SENSr2<sub>extreme</sub> and CTRL<sub>counterpart</sub>, we isolate the sea ice perturbation-induced anomalies in SENSr2<sub>extreme</sub> (shading in Fig. S7c, d in the Supplement) by subtracting CTRL<sub>counterpart</sub> from SENSr2<sub>extreme</sub> and overlay them with the internal variability-induced anomalies in CTRL<sub>counterpart</sub> (contours in Fig. S7d in the Supplement). The sea ice-induced anomalous Rossby wave constructively interferes with the internal variability-induced one over the upstream regions including Northern Europe and Central Siberia, contributing to the enhanced wave propagation to downstream regions with emerging high-pressure anomalies over East Asia in SENSr2<sub>extreme</sub> (Fig. S7d in the Supplement). This critical difference appears to be the key to more frequent ECP\_PPI extremes in the SENSr2 experiment.

To illustrate this point, we used the piecewise PV inversion method to examine the impact of the circulation anomalies in region D (the red box in Fig. 5a) on regional ventilation over eastern China in both the negative EU reanalysis data and modeling data results from SENSr2<sub>extreme</sub> and CTRL<sub>counterpart</sub>. We first partitioned tropospheric PV anomalies into two parts: the lower troposphere (1000-850 hPa) and the middle to upper troposphere (700-100 hPa) and then inverted each PV piece at two levels to estimate the near-surface (850 hPa) horizontal anomalous winds associated with these PV anomalies. We find significantly weakened wind fields in eastern China in both the reanalysis data and SENSr2<sub>extreme</sub>, but not in CTRL<sub>counterpart</sub>. In contrast to strong climatological northwesterly winds over northeastern Asia (Fig. 6a, b, c), PV anomalies in the middle to upper troposphere in both reanalysis-based negative EU and model-based SENSr2<sub>extreme</sub> induce anomalous southeasterly winds at the lower troposphere over the East Asia coastal regions ECP region (Fig. 6e, 6d, e), which is not the case in CTRL<sub>counterpart</sub> (Fig. 6f). These anomalous southeasterlies weaken the monsoon northwesterlies and strengthen air stagnation in this region in the first two cases. We also compare the contribution of PV anomalies at different levels and find that the ventilation suppression effect is dominated by anomalous PV in the middle to upper troposphere (700 hPa and above) rather than that in the lower troposphere (below 700 hPa) in both reanalysis and SENSr2<sub>extreme</sub> data. Comparing to anomalous southerly winds induced by PV anomalies in middle to upper levels (Fig. 6e, 6d, e), those PV anomalies in the lower troposphere mainly tend to strengthen northerly climatological winds over the ECP region, though the circulation patterns in the reanalysis and SENSr2<sub>extreme</sub> results (Fig. 6e, f-6g, h) are quite different from CTRL<sub>counterpart</sub> (Fig. 6i). In general, the ventilation suppression effect associated with middle and upper level circulation PV anomalies overwhelms the enhancement effect associated with lower level PV anomalies and finally suppresses monsoon winds as a net effect (Fig. 6g, h in the reanalysis and SENSr2<sub>extreme</sub> results (Fig. 6j, k), while CTRL<sub>counterpart</sub> manifests an opposite net effect with the dominant role of lower level PV anomalies (Fig. 6l).

### 3.4 Historical simulations and future projections in CMIP6

Lastly, we ~~examined~~ examine the historical simulations and future projections of Arctic SIE and ECP\_PPI under the SSP5-8.5 scenario based on 8 currently available CMIP6 climate models (Eying et al., 2016; see Table S1 in the Supplement for model details) to understand how this teleconnection relationship might change in the future. Figure 7 shows the time series of ~~these two variables~~ the Arctic sea ice and ECP\_PPI and the statistical distribution changes of ECP\_PPI among three time periods: P1 (1951-2000) defined as the reference period with slowly declining Arctic SIE, P2 (2001-2050) as the near-term projection with rapidly decreasing Arctic SIE, and P3 (2051-2100) as the long-term projection with an almost ice-free Arctic in boreal Autumn. A similar figure is available in the Supplement to show the relationship between Arctic SIE change and MCA\_Z500 time series (Fig. S8). Although the CMIP6 model ensemble captures the observed decreasing trend in Arctic SIE, it generally shows less interannual and interdecadal variability of Arctic SIE and ECP\_PPI than the reanalysis data. Low decadal variations in the CMIP6 models are also evident in the CDF distributions of simulated ECP\_PPI. For instance, the simulated ECP\_PPI CDF curve in P1 is positively shifted over the whole distribution range in comparison with the reanalysis-based one (Fig. 7b), while the simulated CDF curve in P2 is negatively shifted relative to the reanalysis data (Fig. 7c) especially over the lower ends of the distribution. Therefore, the shift to positive PPI distributions from P1 to P2 in the NCEP reanalysis data is much more significant than the CMIP6 ensemble-, which is understandable since the reanalysis data is just a single realization and the CMIP6 modeling result is ensemble average. This shrunken interdecadal change in the CMIP6 model ensemble is also found in MCA\_Z500 but to a less prominent extent (Fig. S8b-d in the Supplement). Consequently, the ensemble mean values and averaged probability of simulated ECP\_PPI positive extremes increase from -0.05/5% in P1 to 0.07/7% in P2 (Fig. 7c), which is smaller than those presented in the reanalysis data (-0.38/5% in P1 to 0.30/19% in P2). With the greatest change of Arctic SIE in P3, the ensemble averaged probability of ECP\_PPI positive extremes nearly doubles and increases to 9% with the ECP\_PPI mean value of 0.09 (Fig. 7d), and the ensemble variance of ECP\_PPI projections also increases in concurrence with substantially increased positive extremes of MCA\_Z500 in the same time period (Fig. S8d in the Supplement). The model-specific projections of ECP\_PPI positive extreme probabilities range between 2%-11% in P2, and between 2-13% in P3 (Table S5 and Fig. S7S9 in the Supplement).

For more direct comparison with the CESM-WACCM sensitivity results in previous sections, we specifically looked into the two newer versions of CESM (CESM2 and CESM2-WACCM; Table S1 in the Supplement) that were developed in the same CESM project as the CESM-WACCM model used in this study. The ensemble mean and probability of positive extremes in the low-top CESM2 model increase from -0.07/5% in P1 to 0.20/11% in P2 and to 0.11/13% in P3, while these values in the high-top CESM2-WACCM model increase from 0.03/5% in P1 to 0.36/10% in P2 and to 0.27/6% in P3 (Table S5 and Fig. S7S9 in the Supplement). Both model results are much closer to the changes between P1 and P2 shown in the reanalysis data than the other CMIP6 models. These increments are also more significant than the SENSall results of the sensitivity experiment in this study, which might be attributable to the much stronger climate forcing and fully coupled modeling settings in the CMIP6 simulations.

## 4 Discussion and conclusions

~~In this study, we revisited the~~ The connection between Arctic sea ice decline and winter air stagnation has been re-examined as a cause of pollution extremes in China, and the mechanisms for the teleconnection have been explored. We identified a tropospheric pathway linking the remote sea ice changes in the Arctic to regional circulation and ventilation responses in eastern China based on statistical analysis and diagnosis of atmospheric dynamics using the NCEP reanalysis and climate model sensitivity simulation data. The teleconnection mechanism's evolution can be summarized as follows: In autumn and early winter of recent years, substantial declines in sea ice ~~declined greatly~~ in most regions of the Arctic ~~and~~ significantly increased upward heat fluxes during the same period. These changes in surface boundary conditions, especially those that occurred in the Pacific sector of the Arctic (the East Siberian and Chukchi Seas), induced non-linear responses in the atmosphere during the following winter with producing strengthened eddy kinetic energy fluxes over the mid-latitudes from the northeastern Pacific to North Africa and strong convergence of anomalous transient eddy vorticity fluxes overin the vicinity of Scandinavia. This transient eddy forcing led to positive geopotential height tendencies as well as an anomalous ridge in this region throughout

the troposphere. Constructive interference between eddy-induced wave packets and background flow enhanced wave train propagation across Eurasia, resembling the negative phase of the EU pattern. The high-pressure anomalies over eastern Asia in the middle and upper troposphere of this teleconnection pattern finally weakened boundary-layer air ventilation and exacerbated air stagnation extremes in eastern China by suppressing monsoon northwesterlies and enhancing near surface temperature ~~inversion~~ inversions in this region. Such meteorological conditions ~~were~~ are favorable to air pollutant accumulation and secondary formation.

The occurrence of these teleconnection processes depends on complex interactions between climate disturbances and its internal variability, which are reflected by diverse climate sensitivity responses in the full statistical distributions of circulation and ventilation variables. The largest increase of both the probability (by 120132%) and the intensity (by 3230%) of monthly air stagnation ~~extreme events~~ extremes is found in the experiment driven by sea ice perturbations over the Pacific sector of the Arctic (the East Siberian and Chukchi Seas). We emphasize the importance of a full-distribution evaluation, especially for climate extreme ~~event~~ assessment and attribution, considering vastly ~~different~~ distinct responses between mean conditions and extremes and the tendency of underestimated impacts of climate extremes (Schewe et al., 2019). ~~Next, we discuss~~ We note some relevant ~~aspects~~ issues to our analysis that deserve more attention and further investigations.

Firstly, ~~Petoukhov et al. (2013) proposed a common physical mechanism for the generation of~~ Screen and Simmonds (2014) examined the regional summer weather extremes in the Northern Hemisphere through quasi-resonant amplification (QRA). They argued that these extreme related persistent longitudinal impact of planetary-scale high amplitude circulation patterns with zonal wave numbers  $m = 6, 7,$  or  $8$  might result from the trapping of changes on mid-latitude weather extremes and found distinct relationships between quasi-stationary free synoptic waves with zonal planetary wave numbers  $k \cong m$ . These waveguides favor a subsequent strong QRA of the usually weak quasi-stationary response of anomalies and regional weather extremes in terms of temperature and precipitation. Specifically, they found attenuated (amplified) planetary-wave numbers  $m = 6$  amplitudes accompanying positive temperature extremes (near-average temperature) over eastern Asia that is different from other regions like central Asia and western North America (Screen and Simmonds, 2014). This region-dependent relationship can be attributed to the interaction between anomalous planetary waves and climatological mean thermal and orographic forcing (Petoukhov et al., 2013). Several subsequent studies followed this analytical framework and demonstrated the critical role of QRA in recent warm season extreme weather events (Coumou et al., 2014; Kornhuber et al., 2017; Petoukhov et al., 2016). Though the waves that show quasi-stationary phases. The EU-like teleconnection pattern with zonal wave number  $m = 3$  tends to amplify climatological planetary waves in the upstream regions such as the North Atlantic and Europe but attenuate climatological waves in this work does not support their hypothesis, the working mechanism through wave interference could be similar as shown the downstream regions over central and eastern Asia, leading to regional dynamic and thermodynamic responses as demonstrated in Fig. 5d. It is noted this study. It's worth noting that atmospheric ~~circulation~~ teleconnection patterns like EU with smaller wave numbers might also be excited by quasi-stationary spatially inhomogeneous diabatic sources/sinks and orography other than the thermal forcing associated with the SIC/SST perturbation used in this study. Therefore, we have mainly ~~focus~~ focused on the relative changes of teleconnection occurrence probability between the CTRL and sensitivity experiments to isolate the contributions from this single forcing in the simulated atmospheric system. Multiple atmospheric processes and various forcing source regions associated with different teleconnection pathways might increase the detection difficulty in the whole Arctic perturbation experiment.

Secondly, the climate impacts may vary in response to differing location and magnitude of climate forcing as we found in our regional sensitivity experiments and ~~as this issue is~~ often discussed in other modeling studies (Screen, 2017; Sun et al., 2015; McKenna et al., 2018). The different responses might be attributable to different physical mechanisms and atmospheric processes associated with specific forcing-response relationships. Previous studies proposed multiple pathways of Arctic sea ice impacts on middle-latitude atmospheric circulation through troposphere-stratosphere coupling and/or tropospheric processes only- (Overland et al., 2016). It is an intriguing question to quantify the relative importance of different pathways in different case studies. Screen (2017) proposed that a stratosphere pathway dominated the atmosphere responses to sea ice loss in the Barents-Kara Seas whereas tropospheric processes governed wave train responses to sea ice loss in other regions, which is partly consistent with what we found in this study. Similarly, McKenna et al. (2018) also found opposite effects of the regional sea ice forcing on the stratospheric polar vortex in their full-magnitude and half-magnitude forcing experiments, but the tropospheric responses were different between the two experiments with different forcing magnitudes. They suggested that tropospheric processes become more important than stratospheric pathways as the sea ice loss

magnitude increases (McKenna et al., 2018). Our modeling results indicate that the tropospheric processes are the key to understand the ~~foreeforcing~~-response relationship of interest. However, we ~~can not~~ cannot rule out the possible role of stratospheric changes in midlatitude weather extreme events through stratosphere-troposphere coupling processes (Zhang et al., 2018), and the CESM2 model's sensitivity appears to be stronger when the stratosphere is reasonably resolved in its high-top WACCM version. Multiple dynamic processes and teleconnection pathways associated with different forcing source regions increase the detection difficulty in the whole Arctic perturbation experiment. More detailed sensitivity experiments need to be designed and conducted to evaluate such pathway-dependent effects of Arctic sea ice loss on regional circulation and pollution conditions.

Thirdly, climate responses to Arctic sea ice forcing may also vary on intra-seasonal scales. In a recent study, Lu et al. (2019) revealed an important role of the autumn Arctic sea ice in the phase reversal of the Siberian high in November and December-January. They suggested that the autumn Arctic sea ice loss, especially in the Barents Sea, could induce anomalous upward (downward) surface turbulent heat fluxes in November (December-January). This would strengthen (weaken) the development of the storm track in northeastern Europe and decrease (increase) Ural blockings with accelerated (decelerated) westerlies. With inhibited (enhanced) cold air transport from the Arctic to the Siberian area, a weaker (stronger) Siberian high in November (December-January) would occur thereafter. In our modeling results, we also found significant intra-seasonal variations in simulated atmosphere responses. Figure S8S10 in the Supplement shows weekly evolution of geopotential height tendencies and anomalies in SENSr2 from late November to February. The negative phases of the EU pattern are more prominent in early winter than in late winter. Better understanding of such intra-seasonal variations could benefit seasonal and sub-seasonal forecasts of regional ventilation and pollution potentials.

Last but not the least, the concurrence of multiple climate drivers and their synergistic climate impacts should be considered. Since many other climate factors such as Eurasian snow cover, ENSO, and PDO also show considerable influence on regional circulation and air pollution in China (Chang et al., 2016; Sun et al., 2018; Zhao et al., 2016; Zhao et al., 2018; Zhang et al., 2019; Zou et al., 2017), more studies with concurrent climate drivers could be conducted ~~for to obtain a more~~ comprehensive understanding of climate change impacts. However, these climate drivers may interact with each other ~~with both in either~~ synergistic or antagonistic ~~effectsways~~ (Li et al., 2019). ActiveFully sea ice-ocean-atmosphere coupling also allows more ~~sophisticated~~ interactive dynamic and thermodynamic feedbacks with expanded and enhanced climate responses as suggested by previous studies (Deser et al., 2015; Smith et al., 2017) and by the CMIP6 fully coupled projections in this study. It's a great challenge to distinguish robust and significant responses to climate change from atmospheric internal variability due to relatively low signal-to-noise ratios (Barnes and Screen, 2014). Callahan et al. (2019) estimated less than one signal-to-noise ratio of the forced air stagnation response to internal variability in the CESM-LE historical simulations, demonstrating the dominant role of natural variability in modulating regional circulation and ventilation. Divergent consensus on the climate impact of Arctic amplification on midlatitude severe weather remain an open question for the whole climate science community (Cohen et al., 2020). Therefore, long-term climate simulations with larger ensemble sizes should be conducted to achieve more robust modeling-based findings (Screen and Blackport, 2019). Furthermore, the Arctic sea ice cover reached its historical minimum in the fall of 2012 (Fig. 7a; NSIDC/NASA, 2019). The slowdown of Arctic sea ice loss since then may reflect regional climate internal variability and may have weakened the effect of the Arctic sea ice loss on winter extreme haze occurrence in China in recent years.

## Data availability

The NCEP Reanalysis data is provided by the NOAA/OAR/ESRL PSD, Boulder, Colorado, USA, from their web site at <https://www.esrl.noaa.gov/psd/data/gridded/data.ncep.reanalysis.html> <https://www.esrl.noaa.gov/psd/data/gridded/data.ncep.reanalysis.html> (last access: 18 July, 2019). The MEIC-MIX emission inventory data is available at <http://www.meicmodel.org/dataset-mix> <http://www.meicmodel.org/dataset-mix> (last access: 18 July, 2019). The CMIP6 model outputs are distributed by the Earth System Grid Federation (ESGF) at <https://esgf-node.llnl.gov/search/cmip6/> <https://esgf-node.llnl.gov/search/cmip6/> (last access: 24 October, 2019). All the modeling output data reported in the paper are tabulated in the main text and archived on the GLADE and HPSS file systems managed by the Computational & Information Systems Lab (CISL) of NCAR. The modeling source code and data materials are available upon request, which should be addressed to YZYufei Zou (yufei.zou@pnnl.gov).



## Author contributions

YZ and YW conceived the research idea and designed the climate sensitivity experiments. YZ conducted the modeling experiments and analyzed modeling results with ZX. YZ prepared all the figures and wrote the draft manuscript. All authors discussed the results and revised the manuscript.

## Competing interests.

The authors declare no conflict of interest.

## Acknowledgements

We acknowledge high-performance computing support from Yellowstone ([CISL, 2016](#); ark:/85065/d7wd3xhc) and Cheyenne ([CISL, 2019](#); doi:10.5065/D6RX99HX) provided by NCAR's CISL, sponsored by the National Science Foundation. We thank the Physical Sciences Division (PSD) at the NOAA Earth System Research Laboratory (ESRL) for providing the NCEP/NCAR Reanalysis data. We thank the MEIC team for providing the MEIC-MIX emission inventory data. We acknowledge the World Climate Research Programme, which, through its Working Group on Coupled Modelling, coordinated and promoted CMIP6. We thank the climate modeling groups for producing and making available their model output, the Earth System Grid Federation (ESGF) for archiving the data and providing access, and the multiple funding agencies who support CMIP6 and ESGF. We thank DOE's RGMA program area, the Data Management program, and NERSC for making this coordinated CMIP6 analysis activity possible.

We are also thankful to Robert Black, Yi Deng, and Jian Lu for their helpful discussion to improve the data analysis in this paper.

## Financial support

This work is supported by the National Science Foundation Atmospheric Chemistry Program. ZX is supported by the National Natural Science Foundation of China (project number: 41861144014). YZ, HW, and PR are supported by the U.S. Department of Energy (DOE) Office of Science Regional and Global Model Analysis (RGMA) Program. The Pacific Northwest National Laboratory (PNNL) is operated for DOE by Battelle Memorial Institute under contract DE-AC05-76RL01830. It has not been subjected to any agency review and therefore does not necessarily reflect the views of the Foundation, and no official endorsement should be inferred.

## References

- An, Z., Huang, R.J., Zhang, R., Tie, X., Li, G., Cao, J., Zhou, W., Shi, Z., Han, Y., Gu, Z. and Ji, Y.: Severe haze in Northern China: A synergy of anthropogenic emissions and atmospheric processes, *P. Natl. Acad. Sci. USA*, 116, 8657-8666, <https://doi.org/10.1073/pnas.1900125111>, 2019.
- [Barnes, E. A., and Screen, J. A.: The impact of Arctic warming on the midlatitude jet-stream: Can it? Has it? Will it?, \*WIREs Climate Change\*, 6, 277-286, <https://doi.org/10.1002/wcc.337>, 2015.](#)
- Black, R. X., and McDaniel, B. A.: Diagnostic case studies of the northern annular mode, *J. Climate*, 17, 3990–4004, 2004.
- Cai, W. J., Li, K., Liao, H., Wang, H. J., and Wu, L. X.: Weather conditions conducive to Beijing severe haze more frequent under climate change, *Nat. Clim. Change*, 7, 257–262, <https://doi.org/10.1038/nclimate3249>, 2017.

- Callahan, C. W., Schnell, J. L., and Horton, D. E.: Multi-Index Attribution of Extreme Winter Air Quality in Beijing, China, *J Geophys Res-Atmos.*, 124, 4567-4583, <https://doi.org/10.1029/2018jd029738>, 2019.
- Chang, L., Xu, J., Tie, X., and Wu, J.: Impact of the 2015 El Nino event on winter air quality in China, *Scientific Reports*, 6(1), 34275, <https://doi.org/10.1038/srep34275>, <https://doi.org/10.1038/srep34275>, 2016.
- Cheng, Y., Zheng, G., Wei, C., Mu, Q., Zheng, B., Wang, Z., Gao, M., Zhang, Q., He, K., Carmichael, G. and Pöschl, U.: Reactive nitrogen chemistry in aerosol water as a source of sulfate during haze events in China. *Science Advances*, 2, e1601530, 2016.
- Cohen, J., Screen, J. A., Furtado, J. C., Barlow, M., Whittleston, D., Coumou, D., Francis, J., Dethloff, K., Entekhabi, D., Overland, J., and Jones, J.: Recent Arctic amplification and extreme mid-latitude weather, *Nat. Geosci.* 7, 627-637, 2014.
- Cohen, J., Zhang, X., Francis, J. et al.: Divergent consensus on Arctic amplification influence on midlatitude severe winter weather, *Nat. Clim. Change*, 10, 20–29, <https://doi.org/10.1038/s41558-019-0662-y>, 2020.
- Computational and Information Systems Laboratory (CISL): Yellowstone: IBM iDataPlex System (University Community Computing). Boulder, CO: National Center for Atmospheric Research. <http://n2t.net/ark:/85065/d7wd3xhc>, 2016.
- Computational and Information Systems Laboratory (CISL): Cheyenne: HPE/SGI ICE XA System (University Community Computing). Boulder, CO: National Center for Atmospheric Research. doi:10.5065/D6RX99HX, 2019.
- ~~Natl. Acad. Sci. USA, 111(34), 12331–12336, <https://doi.org/10.1073/pnas.1412797111>, 2014~~
- Dawson, J. P., Bloomer, B. J., Winner, D. A., and Weaver, C. P.: Understanding the meteorological drivers of U.S. particulate matter concentrations in a changing climate, *B. Am. Meteorol. Soc.*, 521-532, <https://doi.org/10.1175/BAMS-D-12-00181.1>, <https://doi.org/10.1175/BAMS-D-12-00181.1>, 2014.
- Deser, C., Sun, L. T., Tomas, R. A., and Screen, J.: Does ocean coupling matter for the northern extratropical response to projected Arctic sea ice loss? *Geophys. Res. Lett.*, 43, 2149-2157, 2016.
- Deser, C., Tomas, R., Alexander, M., and Lawrence, D.: The seasonal atmospheric response to projected Arctic sea ice loss in the late twenty-first century. *J. Climate*, 23, 333–351, doi:10.1175/2009JCLI3053.1, 2010.
- Deser, C., Tomas, R. A., and Sun, L. T.: The role of ocean–atmosphere coupling in the zonal-mean atmospheric response to Arctic sea ice loss, *J. Climate*, 28, 2168-2186, doi:10.1175/JCLI-D-14-00325.1, 2015.
- Ding, A. J., Huang, X., Nie, W., Sun, J. N., Kerminen, V. M., Petaja, T., Su, H., Cheng, Y. F., Yang, X. Q., Wang, M. H., Chi, X. G., Wang, J. P., Virkkula, A., Guo, W. D., Yuan, J., Wang, S. Y., Zhang, R. J., Wu, Y. F., Song, Y., Zhu, T., Zilitinkevich, S., Kulmala, M., and Fu, C. B.: Enhanced haze pollution by black carbon in megacities in China, *Geophys Res Lett.*, 43, 2873-2879, [10.1002/2016gl067745](https://doi.org/10.1002/2016gl067745), 2016.
- Eyring, V., Bony, S., Meehl, G. A., Senior, C. A., Stevens, B., Stouffer, R. J., and Taylor, K. E.: Overview of the Coupled Model Intercomparison Project Phase 6 (CMIP6) experimental design and organization, *Geosci. Model Dev.*, 9, 1937-1958, doi:10.5194/gmd-9-1937-2016, 2016
- Geng, G., Zhang, Q., Tong, D., Li, M., Zheng, Y., Wang, S., and He, K.: Chemical composition of ambient PM<sub>2.5</sub> over China and relationship to precursor emissions during 2005–2012, *Atmos. Chem. Phys.*, 17, 9187-9203, <https://doi.org/10.5194/acp-17-9187-2017>, 2017.
- Guo, S., Hu, M., Zamora, M.L., Peng, J., Shang, D., Zheng, J., Du, Z., Wu, Z., Shao, M., Zeng, L. and Molina, M.J.: Elucidating severe urban haze formation in China. *P. Natl. Acad. Sci. USA*, 111, 17373-17378, 2014.
- Hong, C. P., Zhang, Q., Zhang, Y., Davis, S. J., Tong, D., Zheng, Y. X., Liu, Z., Guan, D. B., He, K. B., and Schellnhuber, H. J.: Impacts of climate change on future air quality and human health in China, *P. Natl. Acad. Sci. USA*, 116, 17193-17200, <https://doi.org/10.1073/pnas.1812881116>, 2019.
- Horton, D. E., Skinner, C. B., Singh, D., and Diffenbaugh, N. S.: Occurrence and persistence of future atmospheric stagnation events, *Nat. Clim. Change*, 4, 698-703, 2014.
- Hoskins, B. J., James, I. N., and White, G. H.: The shape, propagation and mean flow interaction of large scale weather systems, *J. Atmos. Sci.*, 40, 1595-1612, 1983.
- Huang, R. J., Zhang, Y., Bozzetti, C., Ho, K. F., Cao, J. J., Han, Y., Daellenbach, K. R., Slowik, J. G., Platt, S. M., Canonaco, F., Zotter, P., Wolf, R., Pieber, S. M., Bruns, E. A., Crippa, M., Ciarelli, G., Piazzalunga, A., Schwikowski, M., Abbaszade, G., Schnelle-Kreis, J., Zimmermann, R., An, Z., Szidat, S., Baltensperger, U., El Haddad, I., Prévôt, A. S.: High secondary aerosol contribution to particulate pollution during haze events in China, *Nature*, 514, 218-222, 2014.



- IPCC, Field, C.B., Barros, V., Stocker, T.F., Qin, D., Dokken, D.J., Ebi, K.L., Mastrandrea, M.D., Mach, K.J., Plattner, G.-K., Allen, S.K., Tignor, M., and Midgley, P.M. (eds.): Managing the risks of extreme events and disasters to advance climate change adaptation. A special report of working groups I and II of the Intergovernmental Panel on Climate Change. Cambridge University Press, Cambridge, UK, and New York, NY, USA, 582 pp, 2012.
- IPCC, Pörtner, H.-O., Roberts, D.C., Masson-Delmotte, V., Zhai, P., Tignor, M., Poloczanska, E., Mintenbeck, K., Nicolai, M., Okem, A., Petzold, J., Rama, B., and Weyer, N. (eds.): Summary for Policymakers. In: IPCC Special Report on the Ocean and Cryosphere in a Changing Climate. In press, 2019.
- Jia, B., Wang, Y., Yao, Y., and Xie, Y.: A new indicator on the impact of large-scale circulation on wintertime particulate matter pollution over China, *Atmos. Chem. Phys.*, 15, 11919-11929, 2015.
- Kalnay, E., Kanamitsu, M., Kistler, R., Collins, W., Deaven, D., Gandin, L., Iredell, M., Saha, S., White, G., Woollen, J., Zhu, Y., Chelliah, M., Ebisuzaki, W., Higgins, W., Janowiak, J., Mo, K. C., Ropelewski, C., Wang, J., Leetmaa, A., Reynolds, R., Jenne, R., and Joseph, D.: The NCEP/NCAR 40-year reanalysis project, *B. Am. Meteorol. Soc.*, 77, 437-471, doi:10.1175/1520-0477(1996)077<0437:Tnyrp>2.0.Co;2, 1996.
- Kan, H. D., Chen, R. J., and Tong, S. L.: Ambient air pollution, climate change, and population health in China, *Environ. Int.*, 42, 10-19, 2012.
- ~~Kornhuber, K., Petoukhov, V., Petri, S., Rahmstorf, S. and Coumou, D.: Evidence for wave resonance as a key mechanism for generating high amplitude quasi-stationary waves in boreal summer. *Clim. Dyn.*, 49, 1961-1979, <https://doi.org/10.1007/s00382-016-3399-6>, 2017.~~
- Lamarque, J. F., Bond, T. C., Eyring, V., Granier, C., Heil, A., Klimont, Z., Lee, D., Liousse, C., Mieville, A., Owen, B., Schultz, M. G., Shindell, D., Smith, S. J., Stehfest, E., Van Aardenne, J., Cooper, O. R., Kainuma, M., Mahowald, N., McConnell, J. R., Naik, V., Riahi, K., and van Vuuren, D. P.: Historical (1850-2000) gridded anthropogenic and biomass burning emissions of reactive gases and aerosols: methodology and application, *Atmos. Chem. Phys.*, 10, 7017-7039, 10.5194/acp-10-7017-2010, 2010.
- Lau, N.-C. and Holopainen, E. O.: Transient eddy forcing of the time-mean flow as identified by geopotential tendencies, *J. Atmospheric Sci.*, 41, 313-328, <https://doi.org/10.1175/1520-0469, 1984>.
- Lau, N.-C. and Nath, M. J.: Variability of the baroclinic and barotropic transient eddy forcing associated with monthly changes in the midlatitude storm tracks, *J. Atmospheric Sci.*, 48, 2589-2613, 1991.
- Li, B. G., Gasser, T., Ciais, P., Piao, S., Tao, S., Balkanski, Y., Hauglustaine, D., Boisier, J.-P., Chen, Z., Huang, M., Li, L. Z., Li, Y., Liu, H., Liu, J., Peng, S., Shen, Z., Sun, Z., Wang, R., Wang, T., Yin, G., Yin, Y., Zeng, H., Zeng, Z., and Zhou, F.: The contribution of China's emissions to global climate forcing, *Nature*, 531, 357-361, <https://doi.org/10.1038/nature17165>, 2016.
- Li, J., Zheng, F., Sun, C., Feng, J. and Wang, J.: Pathways of influence of the Northern Hemisphere mid-high latitudes on East Asian climate: A review. *Adv. Atmos. Sci.*, 36, 902-921, <https://doi.org/10.1007/s00376-019-8236-5>, 2019.
- Li, M., Zhang, Q., Kurokawa, J.-i., Woo, J.-H., He, K., Lu, Z., Ohara, T., Song, Y., Streets, D. G., Carmichael, G. R., Cheng, Y., Hong, C., Huo, H., Jiang, X., Kang, S., Liu, F., Su, H., and Zheng, B.: MIX: a mosaic Asian anthropogenic emission inventory under the international collaboration framework of the MICS-Asia and HTAP, *Atmos. Chem. Phys.*, 17, 935-963, <https://doi.org/10.5194/acp-17-935-2017>, 2017.
- Li, Y., Sheng, L., Li, C. and Wang, Y.: Impact of the Eurasian teleconnection on the interannual variability of haze-fog in northern China in January, *Atmosphere*, 10, 113, 2019.
- Lim, Y. K.: The East Atlantic/West Russia (EA/WR) teleconnection in the North Atlantic: climate impact and relation to Rossby wave propagation, *Clim. Dynam.*, 44, 3211-3222, 2015.
- Liu, J., Mauzerall, D. L., Chen, Q., Zhang, Q., Song, Y., Peng, W., Klimont, Z., Qiu, X., Zhang, S., Hu, M., Lin, W., Smith, K. R., and Zhu, T.: Air pollutant emissions from Chinese households: A major and underappreciated ambient pollution source, *P. Natl. Acad. Sci. USA*, 113, 7756-7761, 2016.
- Liu, Y., Wang, L., Zhou, W., and Chen, W.: Three Eurasian teleconnection patterns: spatial structures, temporal variability, and associated winter climate anomalies, *Clim. Dyn.*, 42, 2817-2839, DOI:10.1007/s00382-014-2163-z, 2014.
- Lou, S., Yang, Y., Wang, H., Smith, S. J., Qian, Y., and Rasch, P. J.: Black carbon amplifies haze over the North China Plain by weakening the East Asian winter monsoon. *Geophysical Research Letters*, 46(1), 452-460, DOI: 10.1029/2018GL080941, 2019.

- Lu, Z., He, S., Li, F., and Wang, H.: Impacts of the autumn Arctic sea ice on the intraseasonal reversal of the winter Siberian High, *Adv. Atmos. Sci.*, DOI: 10.1007/s00376-017-8089-8, 2019.
- Mann, M.E., Rahmstorf, S., Kornhuber, K., Steinman, B.A., Miller, S.K., Petri, S. and Coumou, D.. Projected changes in persistent extreme summer weather events: The role of quasi-resonant amplification. *Science advances*, 4(10), p.eaat3272, 2018.
- Marsh, D. R., Mills, M. J., Kinnison, D. E., and Lamarque, J.-F.: Climate Change from 1850 to 2005 Simulated in CESM1(WACCM), *J. Climate*, 26, 7372-7391, 2013.
- McKenna, C. M., Bracegirdle, T. J., Shuckburgh, E. F., Haynes, P. H., Joshi, M. M.: Arctic sea-ice loss in different regions leads to contrasting Northern Hemisphere impacts, *Geophys. Res. Lett.*, <https://doi.org/10.1002/2017GL076433>, <https://doi.org/10.1002/2017GL076433>, 2018.
- Niu, F., Li, Z. Q., Li, C., Lee, K. H., and Wang, M. Y.: Increase of wintertime fog in China: Potential impacts of weakening of the Eastern Asian monsoon circulation and increasing aerosol loading, *J Geophys Res-Atmos.*, 115, 2010.
- National Snow and Ice Data Center (NSIDC): Quick facts on Arctic sea ice, <https://nsidc.org/cryosphere/quickfacts/seaice.html>, last access: 15 October, 2019
- NSIDC/NASA: Arctic sea ice minimum, <https://climate.nasa.gov/vital-signs/arctic-sea-ice/>, <https://climate.nasa.gov/vital-signs/arctic-sea-ice/>, last access: 18 July, 2019
- Overland, J. E., Dethloff, K., Francis, J. A., Hall, R. J., Hanna, E., Kim, S. J., Screen, J. A., Shepherd, T. G., and Vihma, T.: Nonlinear response of mid-latitude weather to the changing Arctic, *Nat Clim Change*, 6, 992-999, 10.1038/Nclimate3121, 2016.
- Pei, L., Yan, Z., Sun, Z., Miao, S., and Yao, Y.: Increasing persistent haze in Beijing: potential impacts of weakening East Asian winter monsoons associated with northwestern Pacific sea surface temperature trends, *Atmos. Chem. Phys.*, 18, 3713-3183, <https://doi.org/10.5194/acp-18-3173-2018>, 2018.
- ~~Petoukhov, V., Rahmstorf, S., Petri, S. and Schellnhuber, H.J.: Quasiresonant amplification of planetary waves and recent Northern Hemisphere weather extremes, *P. Natl. Acad. Sci. USA*, 110, 5336-5341, <https://doi.org/10.1073/pnas.1222000110>, 2013.~~
- ~~Petoukhov, V., Petri, S., Rahmstorf, S., Coumou, D., Kornhuber, K. and Schellnhuber, H.J.: Role of quasiresonant planetary wave dynamics in recent boreal spring to autumn extreme events. *P. Natl. Acad. Sci. USA*, 113, 6862-6867, <https://doi.org/10.1073/pnas.1606300113>, 2016.~~
- Rayner, N. A., Parker, D. E., Horton, E. B., Folland, C. K., Alexander, L. V., Rowell, D. P., Kent, E. C., and Kaplan, A.: Global analyses of sea surface temperature, sea ice, and night marine air temperature since the late nineteenth century, *J. Geophys. Res-Atmos.*, 108, 2003.
- Simmons, A. J., Wallace, J. M., and Branstator, G. W.: Barotropic Wave-Propagation and Instability, and Atmospheric Teleconnection Patterns, *J Atmos Sci*, 40, 1363-1392, 1983.
- Schewe, J., Gosling, S.N., Reyer, C., Zhao, F., Ciais, P., Elliott, J., Francois, L., Huber, V., Lotze, H.K., Seneviratne, S.I. and Van Vliet, M.T.: State-of-the-art global models underestimate impacts from climate extremes. *Nature communications*, 10, 1005, <https://doi.org/10.1038/s41467-019-08745-6>, <https://doi.org/10.1038/s41467-019-08745-6>, 2019.
- Screen, J. A.: Simulated atmospheric response to regional and pan-Arctic sea ice loss, *J. Climate*, 30, 3945-3962, 2017.
- Screen, J. A., and Blackport, R.: How Robust is the Atmospheric Response to Projected Arctic Sea Ice Loss Across Climate Models?, *Geophys Res Lett*, 46, 11406-11415, 10.1029/2019gl084936, 2019.
- Screen, J. A., and Simmonds, I.: Amplified mid-latitude planetary waves favour particular regional weather extremes, *Nat. Clim. Change*, 4, 704-709, <https://doi.org/10.1038/nclimate2271>, 2014.
- Screen, J. A., Simmonds, I., Deser, C., and Tomas, R.: The atmospheric response to three decades of observed arctic sea ice loss, *J. Climate*, 26, 1230-1248, DOI: 10.1175/JCLI-D-12-00063.1, 2013.
- Song, C. B., Wu, L., Xie, Y. C., He, J. J., Chen, X., Wang, T., Lin, Y. C., Jin, T. S., Wang, A. X., Liu, Y., Dai, Q. L., Liu, B. S., Wang, Y. N., and Mao, H. J.: Air pollution in China: Status and spatiotemporal variations, *Environ. Pollut.*, 227, 334-347, <https://doi.org/10.1016/j.envpol.2017.04.075>, 2017.
- Sun, J., Li, H., Zhang, W., Li, T., Zhao, W., Zuo, Z., Guo, S., Wu, D., Fan, S.: Modulation of the ENSO on winter aerosol pollution in the eastern region of China, *J. Geophys. Res-Atmos.*, 123, <https://doi.org/10.1029/2018JD028534>, 2018.
- Sun, L., Deser, C., and Tomas, R.A.: Mechanisms of stratospheric and tropospheric circulation response to projected Arctic sea ice loss, *J. Climate*, 28, 7824-7845, DOI: <https://doi.org/10.1175/JCLI-D-15-0169.1>, 2015.

- Sun, Y. L., Du, W., Fu, P., Wang, Q., Li, J., Ge, X., Zhang, Q., Zhu, C., Ren, L., Xu, W., Zhao, J., Han, T., Worsnop, D. R., and Wang, Z.: Primary and secondary aerosols in Beijing in winter: sources, variations and processes, *Atmos. Chem. Phys.*, 16, 8309-8329, 2016.
- Takaya, K., and Nakamura, H.: A formulation of a phase-independent wave-activity flux for stationary and migratory quasigeostrophic eddies on a zonally varying basic flow, *J. Atmos. Sci.*, 58, 608-627, 2001.
- ~~Taylor, K. E., Stouffer, R. J., and Meehl, G. A.: An Overview of Cmp5 and the Experiment Design, *B. Am. Meteorol. Soc.*, 93, 485-498, 2012.~~
- The State Council of the People's Republic of China: Notice on the air pollution prevention and control action plan, ~~[http://www.gov.cn/zwgc/2013-09/12/content\\_2486773.htm](http://www.gov.cn/zwgc/2013-09/12/content_2486773.htm)~~ (2013)-[http://www.gov.cn/zwgc/2013-09/12/content\\_2486773.htm](http://www.gov.cn/zwgc/2013-09/12/content_2486773.htm), 2013, last access: 1 August, 2019.
- Trenberth, K. E.: An assessment of the impact of transient eddies on the zonal flow during a blocking episode using localized Eliassen-Palm flux diagnostics, *J. Atmos. Sci.*, 43, 2070-2087, 1986.
- Wallace, J. M. and Gutzler, D. S.: Teleconnections in the geopotential height field during the Northern Hemisphere winter, *Mon. Weat. Rev.*, 109, 784-812, 1981.
- Wang, G. H., Zhang, R., Gomez, M. E., Yang, L., Zamora, M. L., Hu, M., Lin, Y., Peng, J., Guo, S., Meng, J., Li, J., Cheng, C., Hu, T., Yanqin Ren, Y., Wang, Y., Gao, J., Cao, J., An, Z., Zhou, W., Li, G., Wang, J., Tian, P., Marrero-Ortiz, W., Secrest, J., Du, Z., Zheng, J., Shang, D., Zeng, L., Shao, M., Wang, W., Huang, Y., Wang, Y., Zhu, Y., Li, Y., Hu, J., Pan, B., Cai, L., Cheng, Y., Ji, Y., Zhang, F., Rosenfeld, D., Liss, P. S., Duce, R. A., Kolb, C. E., and Molina, M. J.: Persistent sulfate formation from London fog to Chinese haze, *P. Natl. Acad. Sci. USA*, 113, 13630-13635, 2016.
- Wang, H. J., and Chen, H.-P.: Understanding the recent trend of haze pollution in eastern China: roles of climate change, *Atmos. Chem. Phys.*, 16, 4205-421, 2016.
- Wang, H. J., Chen, H. P., and Liu, J. P.: Arctic sea ice decline intensified haze pollution in eastern China, *Atmos. Ocean. Sci. Lett.*, 8, 1-9, 2015.
- Wang, N. and Zhang, Y.: Evolution of Eurasian teleconnection pattern and its relationship to climate anomalies in China, *Clim. Dyn.*, 45, 1017-1028, DOI:10.1007/s00382-014-2171-z, 2015.
- Wilks, D. S.: Statistical methods in the atmospheric sciences. International geophysics series, ed. 3rd, Academic Press, Oxford Waltham, MA, pp. xix, 676 p, 2011.
- Wu, B., Su, J., and D'Arrigo, R.: Patterns of Asian winter climate variability and links to Arctic sea ice, *J. Climate*, 28, 6841-6858, 2015.
- Xie, Y., Dai, H. C., Dong, H. J., Hanaoka, T., and Masui, T.: Economic impacts from PM2.5 pollution-related health effects in China: A provincial-level analysis, *Environ. Sci. Technol.*, 50, 4836-4843, 2016.
- ~~Xie, Z., Black, R. X., and Deng, Y.: Planetary and synoptic-scale dynamic control of extreme cold wave patterns over the United States, *Clim. Dyn.*, 53, 1477-1495, <https://doi.org/10.1007/s00382-019-04683-7>, 2019.~~
- Yin, Z. and Wang, H.: Role of atmospheric circulations in haze pollution in December 2016, *Atmos. Chem. Phys.*, 17, 11673-11681, 2017.
- Yin, Z. and Wang, H. J.: The strengthening relationship between Eurasian snow cover and December haze days in central North China after the mid-1990s, *Atmos. Chem. Phys.*, 18, 4753-4763, <https://doi.org/10.5194/acp-18-4753-2018>, <https://doi.org/10.5194/acp-18-4753-2018>, 2018.
- Zhao, S., Zhang, H., and Xie, B.: The effects of El Niño–Southern Oscillation on the winter haze pollution of China. *Atmos. Chem. Phys.*, 18, 1863–1877, <https://doi.org/10.5194/acp-18-1863-2018>, <https://doi.org/10.5194/acp-18-1863-2018>, 2018.
- Zhao, S., Li, J., and Sun, C.: Decadal variability in the occurrence of wintertime haze in central eastern China tied to the Pacific Decadal Oscillation, *Scientific Reports*, 6(1), 27424, <https://doi.org/10.1038/srep27424>, <https://doi.org/10.1038/srep27424>, 2016.
- Zhang, P., Wu, Y., Simpson, I.R., Smith, K.L., Zhang, X., De, B. and Callaghan, P.: A stratospheric pathway linking a colder Siberia to Barents-Kara Sea sea ice loss. *Science advances*, 4, eaat6025, <https://doi.org/10.1126/sciadv.aat6025>, 2018.
- Zhang, G., Gao, Y., Cai, W., Leung, L. R., Wang, S., Zhao, B., Wang, M., Shan, H., Yao, X., and Gao, H.: Seesaw haze pollution in North China modulated by the sub-seasonal variability of atmospheric circulation, *Atmos. Chem. Phys.*, 19, 565-576, <https://doi.org/10.5194/acp-19-565-2019>, 2019.
- Zhang, Q., Zheng, Y. X., Tong, D., Shao, M., Wang, S. X., Zhang, Y. H., Xu, X. D., Wang, J. N., He, H., Liu, W. Q., Ding, Y. H., Lei, Y., Li, J. H., Wang, Z. F., Zhang, X. Y., Wang, Y. S., Cheng, J., Liu, Y., Shi, Q. R., Yan, L., Geng, G. N., Hong, C. P., Li, M., Liu, F., Zheng, B., Cao, J. J., Ding, A. J., Gao, J., Fu, Q. Y.,

- [Huo, J. T., Liu, B. X., Liu, Z. R., Yang, F. M., He, K. B., and Hao, J. M.: Drivers of improved PM2.5 air quality in China from 2013 to 2017, \*P. Natl. Acad. Sci. USA\*, 116, 24463-24469, <https://doi.org/10.1073/pnas.1907956116>, 2019.](https://doi.org/10.1073/pnas.1907956116)
- [Zhang, X., Zhong, J., Wang, J., Wang, Y., and Liu, Y.: The interdecadal worsening of weather conditions affecting aerosol pollution in the Beijing area in relation to climate warming, \*Atmos. Chem. Phys.\*, 18, 5991-5999, <https://doi.org/10.5194/acp-18-5991-2018>, 2018.](https://doi.org/10.5194/acp-18-5991-2018)
- Zhong, J., Zhang, X., Dong, Y., Wang, Y., Liu, C., Wang, J., Zhang, Y., and Che, H.: Feedback effects of boundary-layer meteorological factors on cumulative explosive growth of PM2.5 during winter heavy pollution episodes in Beijing from 2013 to 2016, *Atmos. Chem. Phys.*, 18, 247-258, <https://doi.org/10.5194/acp-18-247-2018>, 2018.
- Zou, Y., Wang, Y., Zhang, Y., and Koo, J.-H.: Arctic sea ice, Eurasia snow, and extreme winter haze in China, *Science Advances*, 3, e1602751, <https://doi.org/10.1126/sciadv.1602751>, 2017.

|

**Table 1.1. The modeling settings of the climate sensitivity experiments using CESM-WACCM**

Experiment	CTRL	SENSall	SENSr1	SENSr2	SENSr3
Time period	30 years	30 years	30 years	30 years	30 years
Horizontal resolution	1.9°×2.5°	1.9°×2.5°	1.9°×2.5°	1.9°×2.5°	1.9°×2.5°
Vertical level	70	70	70	70	70
Atmosphere	WACCM <sup>(a)</sup>	WACCM	WACCM	WACCM	WACCM
Land	CLM4.0	CLM4.0	CLM4.0	CLM4.0	CLM4.0
Ocean	Climatology <sup>(b)</sup>	2012 Arctic SST	2012 R1 SST <sup>(c)</sup>	2012 R2 SST	2012 R3 SST
Sea ice	Climatology <sup>(b)</sup>	2012 Arctic SIC	2012 R1 SIC	2012 R2 SIC	2012 R3 SIC
China emissions	MEIC-MIX	MEIC-MIX	MEIC-MIX	MEIC-MIX	MEIC-MIX
Other emissions	IPCC AR5	IPCC AR5	IPCC AR5	IPCC AR5	IPCC AR5

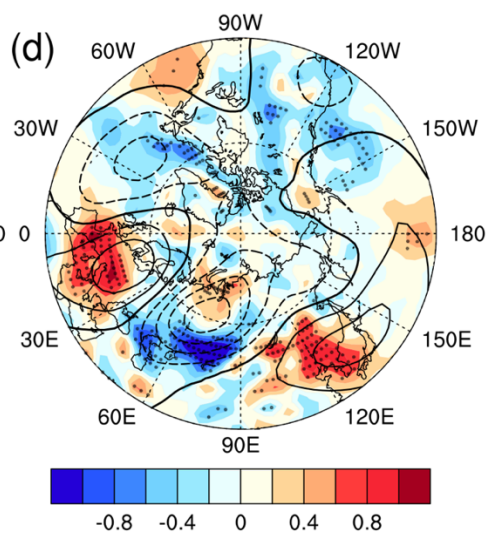
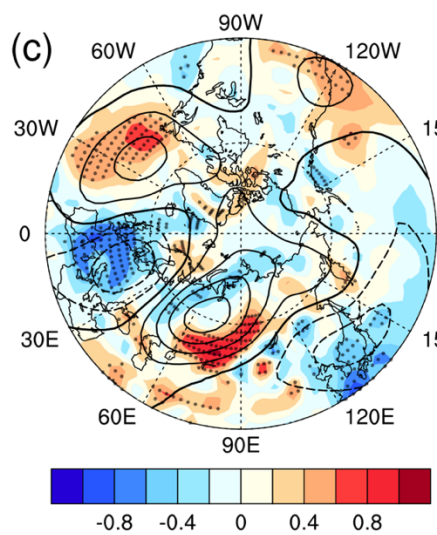
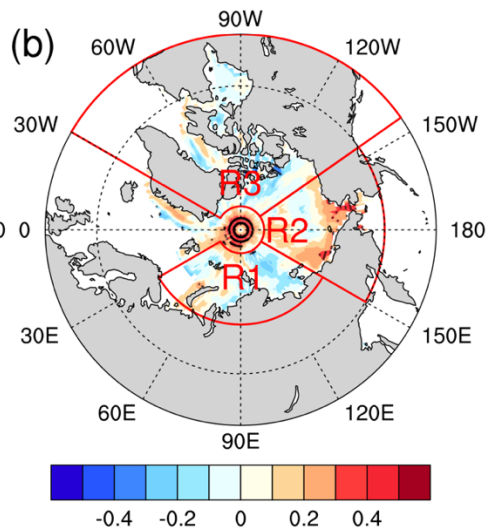
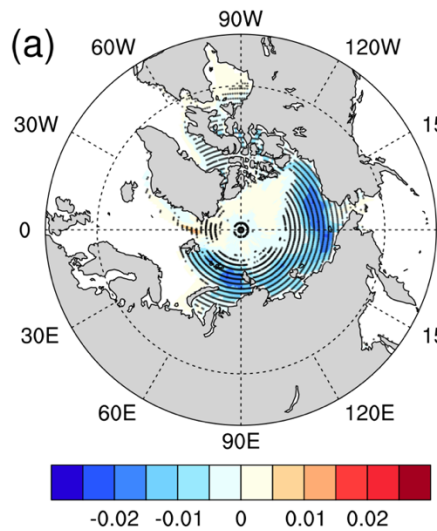
<sup>(a)</sup>: using CAM5 physics package and WACCM\_MOZART\_MAM3 chemistry package;

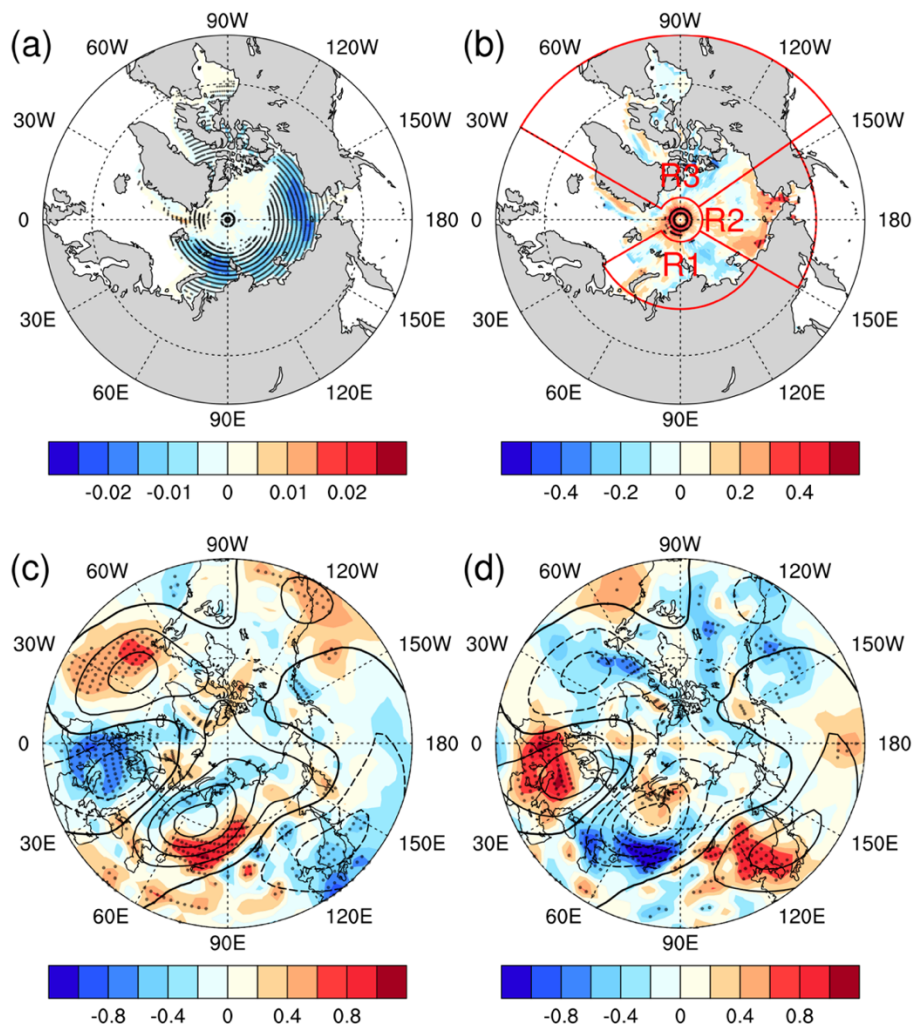
<sup>(b)</sup>: 1981-2010 average based on the HadISST SST and SIC data (Rayner et al., 2003);

<sup>(c)</sup>: see the main text and Fig. 1b for the R1-R3 region definition;

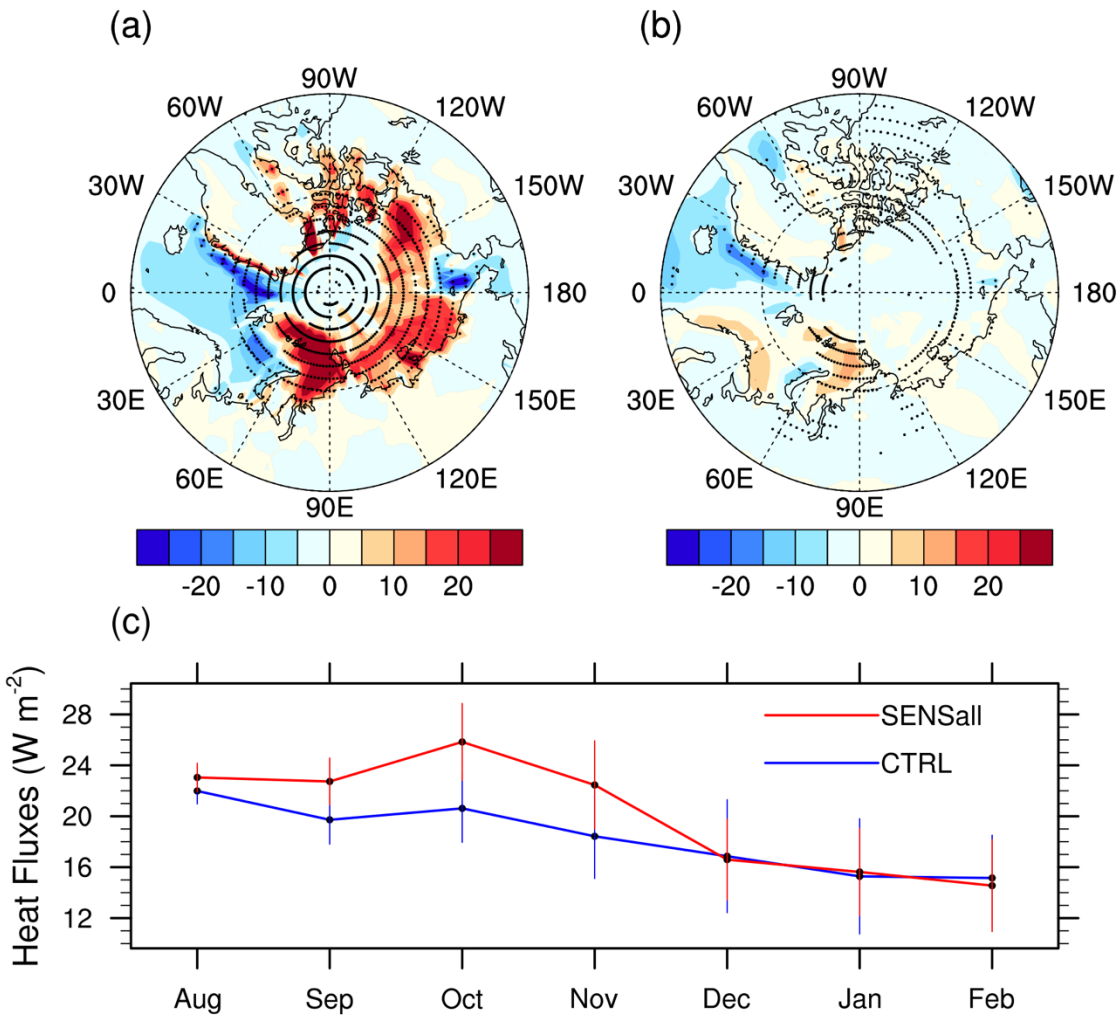


|

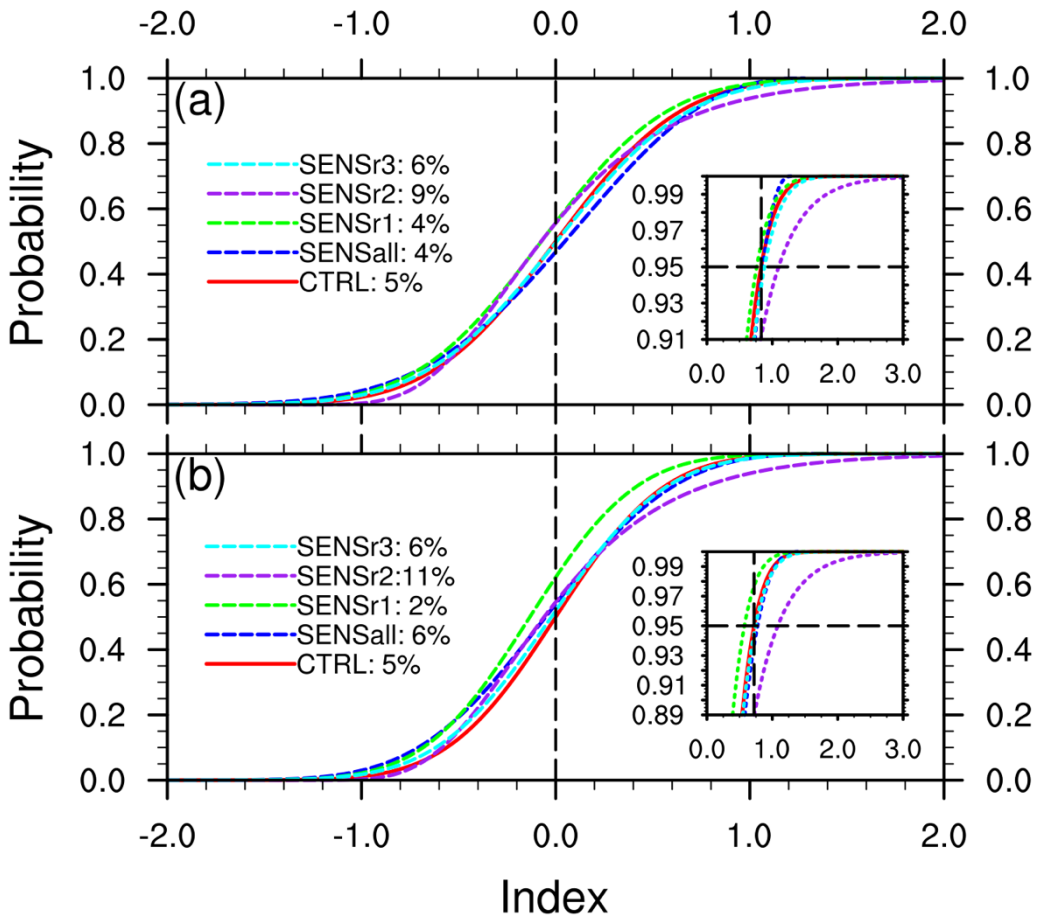


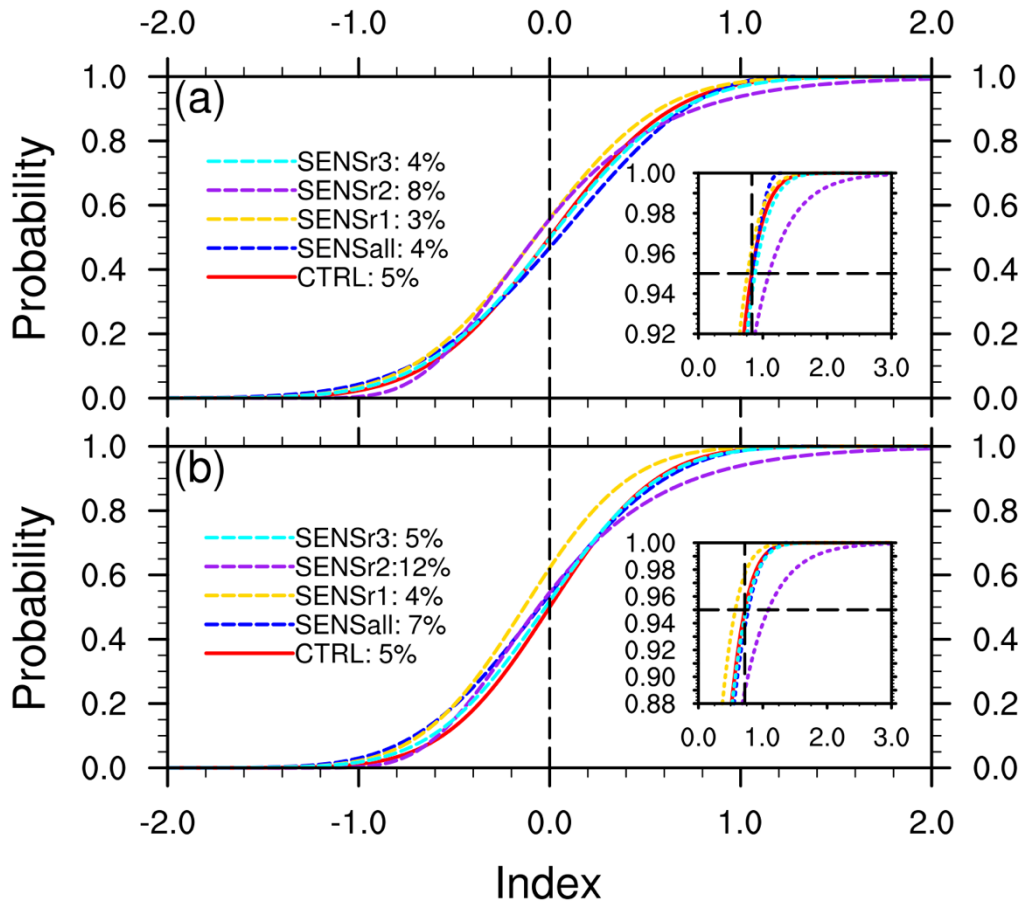


**Figure 4.1.** Relationship between Arctic sea ice changes, EU teleconnection, and pollution ventilation conditions in the Northern Hemisphere: based on the reanalysis and observational data. (a) trends of Arctic sea ice changes in autumn and early winter (ASON) of 1980-2017 (color shading in the Arctic region, year<sup>-1</sup>); (b) correlation between the winter EU index and preceding Arctic sea ice concentrations (color shading in the Arctic region, unitless); R1-3 denote the perturbation regions in the three region-specific sensitivity experiments; (c) PPI spatial distributions (color shading, unitless) during the positive phase of EU (contours with interval of 20 m; dashed/solid lines indicate negative/positive geopotential heights at 500 hPa); (d) PPI spatial distributions (color shading, unitless) during the negative phase of EU (contours with interval of 20 m; dashed/solid lines indicate negative/positive geopotential heights at 500 hPa). The black dots/stipples over color shading denote the 0.05 significance level based on the two-tailed Student's t-test.



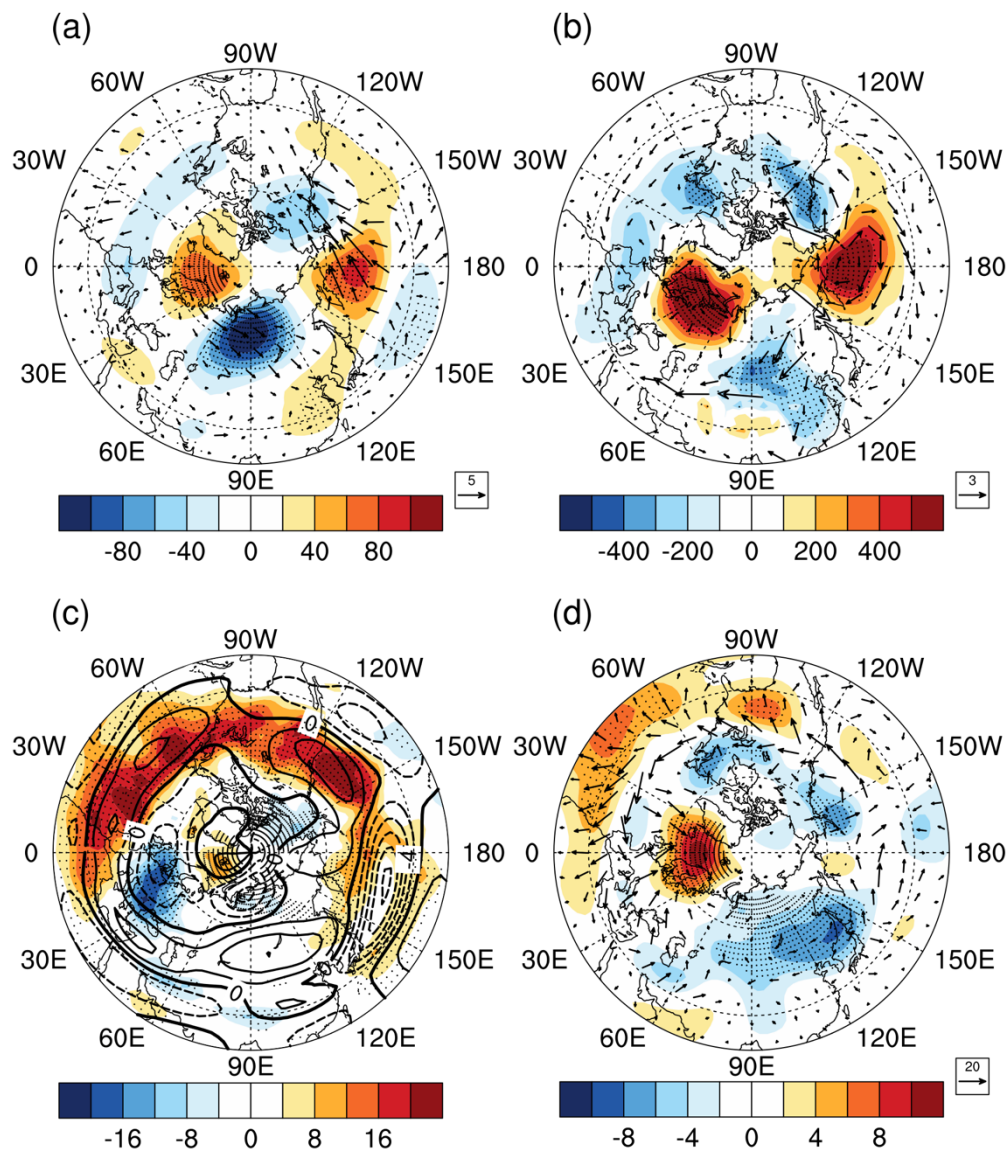
**Figure 2.2.** Surface heat flux changes over the Arctic in the WACCM SENSall simulation. (a) differences of surface sensible plus latent heat fluxes (positive upward) between SENSall and CTRL during Aug-Nov; (b) differences of surface sensible plus latent heat fluxes between SENSall and CTRL during Dec-Feb; (c) comparison of regional averaged surface heat fluxes over the Arctic (north of 66.6° N) from August to February. The **black dots/stipples** in (a)/(b) denote the 0.05 significance level. The error bars in (c) denote one standard deviation of the 30-member ensembles in CTRL and SENSall, respectively.





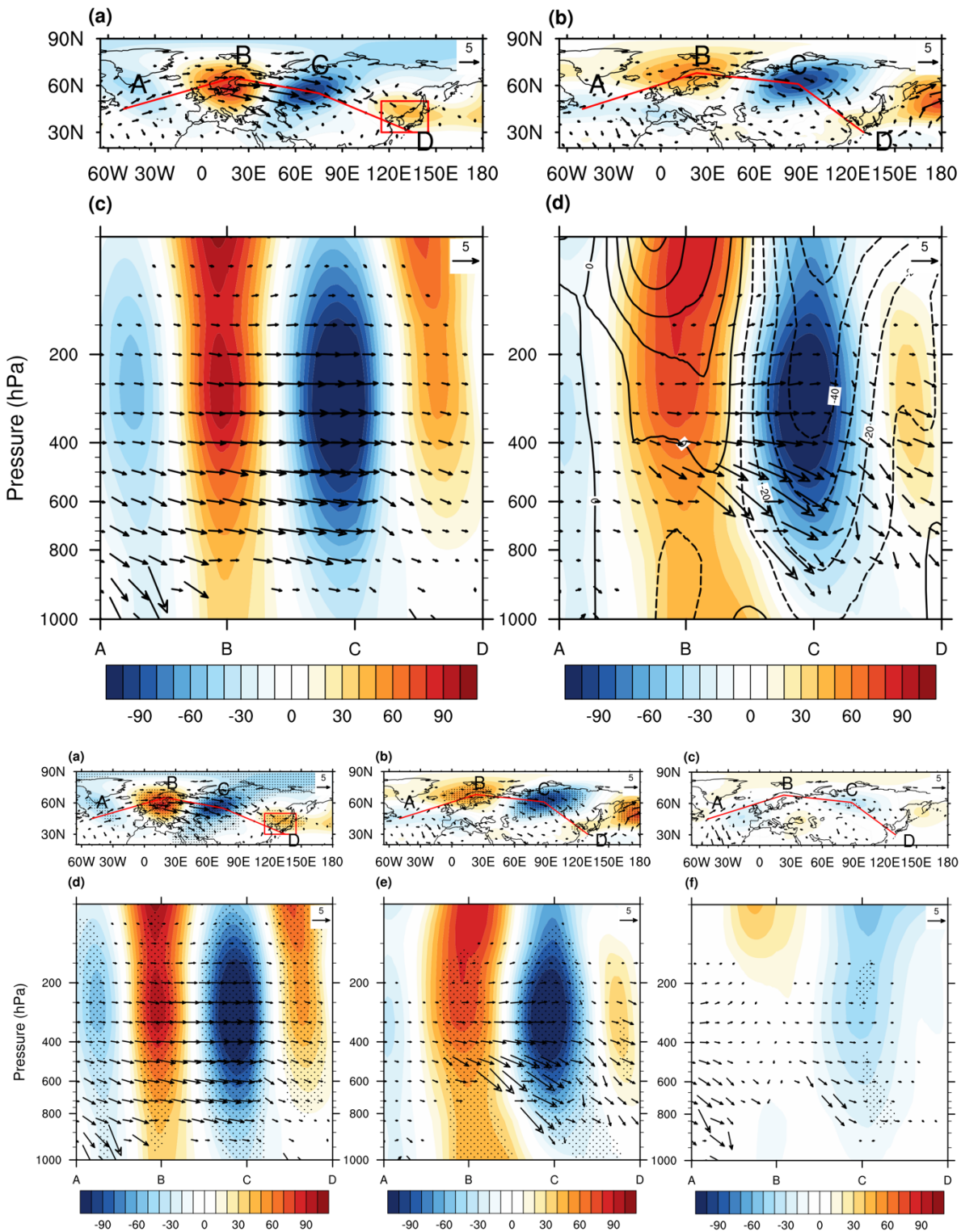
**Figure 3. Atmospheric3. Comparison of the statistical distributions of atmospheric circulation and regional air stagnation responses to the Arctic sea ice forcing indices in the WACCM climate sensitivity experiments. (a) comparison of cumulative distribution functions (CDFs) of the MCA\_Z500 index in winter months (Dec, Jan, and Feb). The percentages in the legend are the occurrence probabilities of positive extreme members; the inset shows the zoomed-in distributions of positive MCA\_Z500 extremes ( $\geq MCA\_Z500_{CTRL}^{95th}$ ) and the black dashed lines in the inset denote the positive extreme threshold ( $MCA\_Z500_{CTRL}^{95th} = 0.83$ ); (b) same as (a) but for the regional averaged ECP\_PPI index; the inset shows the zoomed-in distributions of positive PPI extremes ( $\geq ECP\_PPI_{CTRL}^{95th}$ ) and the black dashed lines in the inset denote the positive extreme threshold ( $ECP\_PPI_{CTRL}^{95th} = 0.72$ ).**





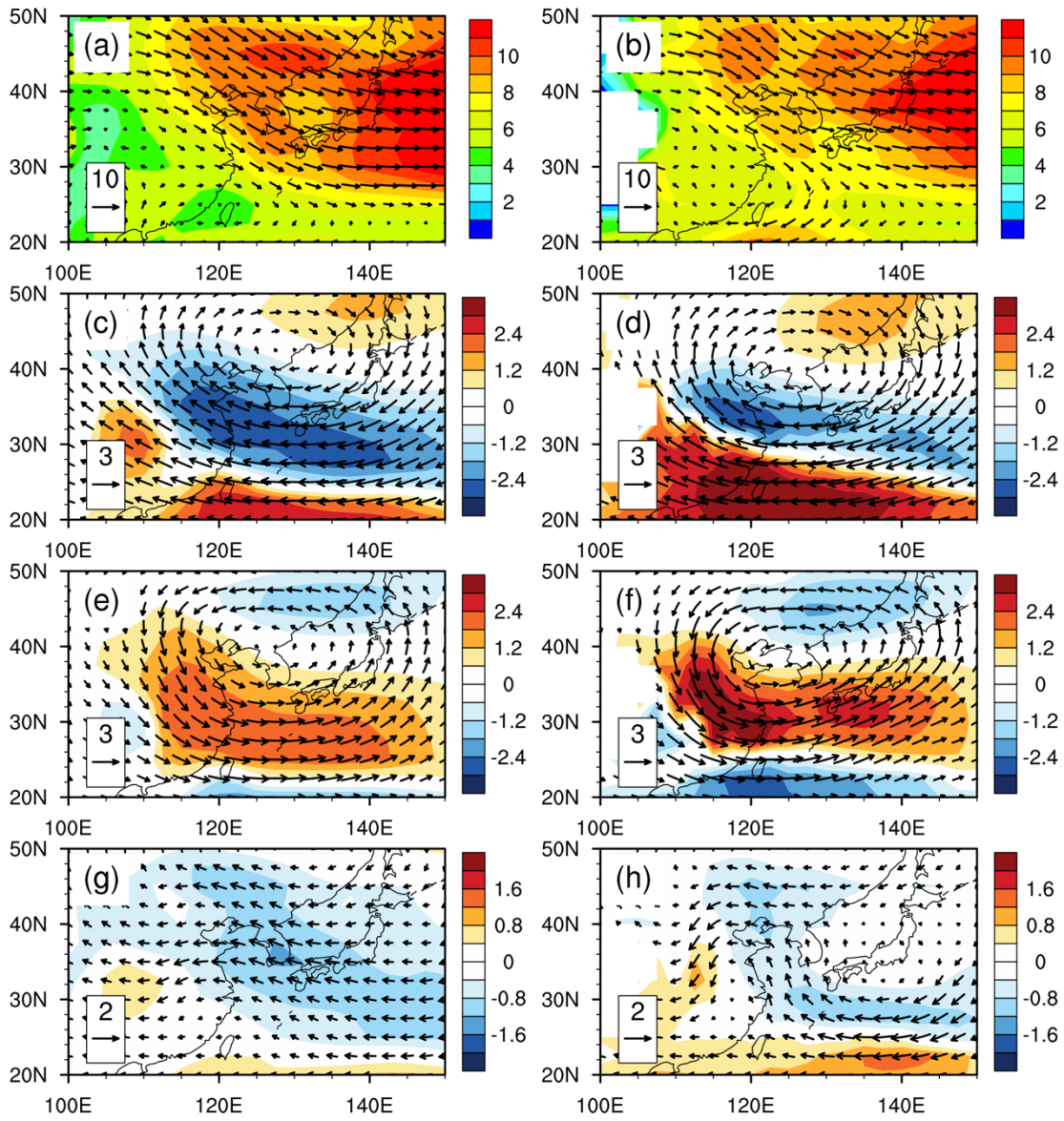
**Figure 4. Winter atmospheric responses to the autumn and early winter sea ice change in the Pacific sector of the Arctic** **Figure 4. Atmospheric anomalies** in WACCM SENSr2 extreme members with respect to the CTRL ensemble mean. (a) geopotential height (color shading, m) and wave activity flux (vectors,  $\text{m}^2 \text{s}^{-2}$ ) anomalies at 250 hPa; (b) sea level pressure (color shading, Pa) and surface wind circulation (vectors,  $\text{m s}^{-1}$ ) anomalies; (c) Anomalous transient eddy kinetic energy (color shading,  $\text{m}^2 \text{s}^{-2}$ ) and zonal wind (contours,  $\text{m s}^{-1}$ ) anomalies at 250 hPa; (d) Anomalous E vectors (vectors,  $\text{m}^2 \text{s}^{-2}$ ) and transient eddy-induced geopotential height tendencies ( $Z_t^{V+H}$ ) (color shading,  $\text{m day}^{-1}$ ) at 250 hPa. The **black dots/stipples** denote the 0.05 significance level.

|



**Figure 5.5.** Comparison of the EU pattern atmospheric anomalies in the NCEP reanalysis data and WACCM SENSr2 extreme members experiments. (a) reanalysis-based ensemble mean geopotential heights at 500 hPa (color shading, m) and wave activity flux (WAF) at

250 hPa (vectors,  $\text{m}^2 \text{s}^{-2}$ ) of the 30 strongest negative EU months in winter (DJF) of 1951-2019; (relative to the 1981-2010 climatology); (b) same as (a) but based on the ~~differences between the~~ SENSr2 extreme members and (relative to CTRL ensemble mean); (c) same as (b) but based on the CTRL counterparts of the SENSr2 extreme members (relative to the CTRL ensemble mean); (d) reanalysis-based vertical cross section of geopotential heights (color shading, m) and WAF (vectors,  $\text{m}^2 \text{s}^{-2}$ ) of the ensemble mean negative EU months (relative to the 1981-2010 climatology) along the wave propagation path shown in (a); ~~(e)~~ same as (e) but based on the ~~differences between the~~ SENSr2 extreme members and (relative to the CTRL ensemble mean. The contours in (d) denote the geopotential height anomaly in); (f) same as (e) but based on the counterpart CTRL members counterparts of these the SENSr2 extreme members. (relative to the CTRL ensemble mean). Note that the vertical components of WAF in (c)-(d) were scaled up by 200 for clear illustration. The stipples denote the 0.05 significance level.





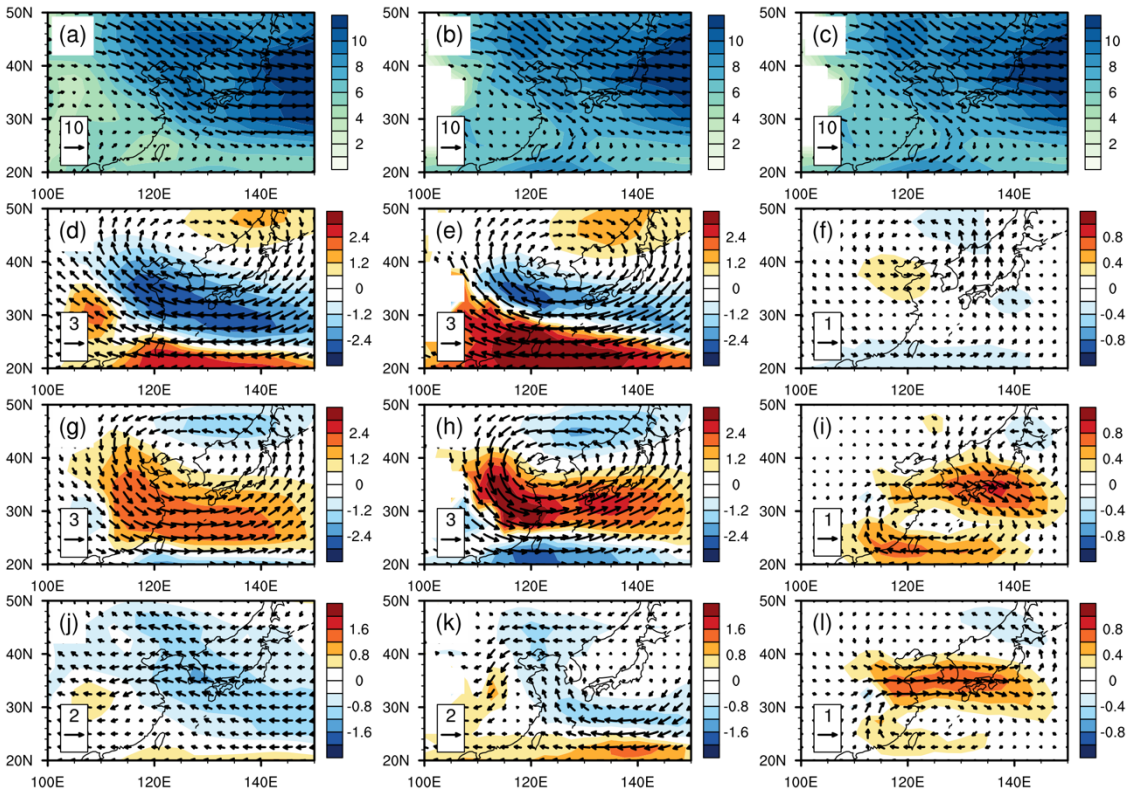


**Figure 6-6.** Comparison of winter circulation in East Asia based on the piecewise PV inversion analysis with the NCEP reanalysis and WACCM experiments modeling data. (a) climatological wind speed (color shading, m) and directions (vector, m) at 850 hPa based on the reanalysis data; (b)-(c) same as (a) but based on the WACCM CTRL ensemble mean; (d) reanalysis-based wind circulation changes at 850 hPa induced by East Asia PV anomalies (see the red box in Fig. 5a) in the middle to upper troposphere (700-100 hPa) during strong negative EU months in winter; (e) model-based wind circulation changes at 850 hPa associated with the middle to upper troposphere PV changes anomalies over East Asia between in the SENSr2 extreme members and (relative to the CTRL ensemble mean); (f) same as (e) but in the CTRL counterparts of the SENSr2 extreme members (relative to the CTRL ensemble mean); (g) reanalysis-based wind circulation changes at 850 hPa induced by East Asia PV anomalies in the lower troposphere (1000-850 hPa) during strong negative EU months in winter; (h) model-based wind circulation changes at 850 hPa associated with the lower troposphere PV changes between anomalies in the SENSr2 extreme members and (relative to CTRL ensemble mean); (i) same as (h) but in the CTRL counterparts of the SENSr2 extreme members (relative to the CTRL ensemble mean); (j) reanalysis-based wind circulation changes at 850 hPa induced by East Asia PV anomalies in the whole troposphere (1000-100 hPa) during strong negative EU months in winter; (k) model-based wind circulation changes at 850 hPa associated with the whole troposphere PV changes between anomalies in the SENSr2 extreme members and (relative to the CTRL ensemble

**mean.); (l) same as (k) but in the CTRL counterparts of the SENSr2 extreme members (relative to the CTRL ensemble mean).**



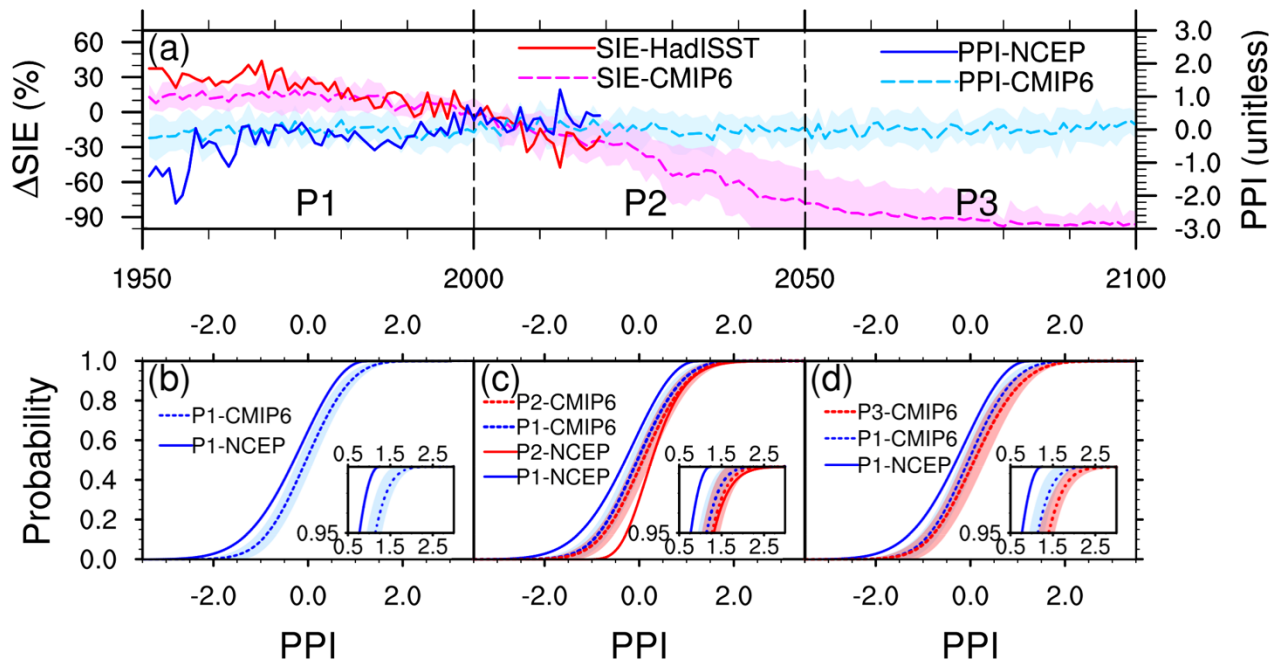


**Figure 7.7.** Historical simulations and future projections (under the SSP5-8.5 scenario) of Arctic sea ice and regional air stagnation in observational and reanalysis data and CMIP6 models. (a) time series of the Arctic SIE relative changes (unit: %; relative to [the 1981-2010 climatology](#)) in preceding September and ECP\_PPI (unitless) in DJF of the following winter (using years of January for X-axis labeling). The solid lines denote observation- and reanalysis-based Arctic SIE and ECP\_PPI from 1950 to 2019. The dashed lines denote ensemble mean and the color shading denotes  $\pm 1$  standard deviation of the 8 CMIP6 models (see Table S1 for model details) from 1950 to 2100. Note that the SIE time series were shifted one year after to be aligned with the ECP\_PPI data; (b) comparison of ECP\_PPI CDF curves between the NCEP reanalysis data and the CMIP6 models in the P1 time period from 1951 to 2000. The [inset](#) denotes the distributions of positive [extreme events](#) ( $\geq PPI_{P1}^{95^{th}}$ ). The color shading denotes  $\pm 1$  standard deviations in the 8 CMIP6 models; (c) Same as (b) but for the comparison between P1 and P2 (2001-2050) time periods as well as between the NCEP reanalysis data and the CMIP6 models; (d) same as (b) but for the comparison between P1 and P3 (2051-2100) time periods as well as between the NCEP reanalysis data and the CMIP6 models. The model-specific comparison in (b)-(d) are shown in Table S5 and Fig. [S7S9](#) in the Supplement.